A Generalized Mixing Length Closure for Eddy-Diffusivity Mass-Flux Schemes of Turbulence and Convection

Ignacio Lopez-Gomez[1], Yair Cohen[1], Jia He[1], Anna Jaruga[1,2], Tapio Schneider[1,2]

[1]California Institute of Technology, Pasadena, California, USA.
[2]Jet Propulsion Laboratory, California Institute of Technology, Pasadena, California, US

Key Points:

- EDMF schemes represent boundary-layer (BL) turbulence and convection separately, yet consistently.
- A mixing length model based on kinetic energy constraints represents turbulent fluxes in EDMF schemes well.
- The resulting EDMF scheme captures dynamic regimes ranging from stable BLs to stratocumulus-topped BLs.

Corresponding author: Tapio Schneider, tapio@caltech.edu

Abstract

Because of their limited spatial resolution, numerical weather prediction and climate models have to rely on parameterizations to represent atmospheric turbulence and convection. Historically, largely independent approaches have been used to represent boundary layer turbulence and convection, neglecting important interactions at the subgrid scale. Here we build on an eddy-diffusivity mass-flux (EDMF) scheme that represents all subgrid-scale mixing in a unified manner, partitioning subgrid-scale fluctuations into contributions from local diffusive mixing and coherent advective structures and allowing them to interact within a single framework. The EDMF scheme requires closures for the interaction between the turbulent environment and the plumes and for local mixing. A second-order equation for turbulence kinetic energy (TKE) provides one ingredient for the diffusive local mixing closure, leaving a mixing length to be parameterized. A new mixing length formulation is proposed, based on constraints derived from the TKE balance. It expresses local mixing in terms of the same physical processes in all regimes of boundary layer flow. The formulation is tested at a range of resolutions and across a wide range of boundary layer regimes, including a stably stratified boundary layer, a stratocumulus-topped marine boundary layer, and dry convection. Comparison with large eddy simulations (LES) shows that the EDMF scheme with this diffusive mixing parameterization accurately captures the structure of the boundary layer and clouds in all cases considered.

Plain Language Summary

Turbulence and convection transport heat and moisture in the atmosphere and are ultimately responsible for the formation of clouds. However, they act on scales far too small to be resolved in current global atmosphere models. Instead, parameterizations have to be used to approximate their average effect on the finite volumes that are resolved in a global model. These parameterizations are often tailored to specific atmospheric conditions and fail when those conditions are not met. Here we propose a parameterization that aims to reproduce the average effect of turbulent heat and moisture transport under arbitrary atmospheric conditions. Numerical simulations demonstrate the accuracy of the parameterization in simulating turbulence in atmospheric boundary layers under stable and convective conditions, including the simulation of stratocumulus clouds.

1 Introduction

Turbulence is ubiquitous in the planetary boundary layer. Small-scale chaotic air motions enhance mixing, homogenizing temperature and water content in the lower troposphere. Under statically unstable conditions, convective updrafts and downdrafts further increase the vertical transport of heat and moisture between the surface and the air aloft. Together, turbulence and convection shape the vertical distribution of temperature and water vapor that sustains clouds. However, these processes act on scales far too small to be resolved in global climate models (GCMs), with resolutions constrained by current computational power (Schneider et al., 2017). Although the unabated increase in processing power will make resolving deep convective processes possible in the coming years (Kajikawa et al., 2016), resolving turbulent mixing and shallow convection will remain an intractable problem for decades. Instead, parameterizations have to be used to approximate the average effect of these subgrid-scale processes on the grid scale.

Conventional parameterizations consider atmospheric turbulence and convection as independent processes, neglecting interactions that alter their combined effect on the large scale. These parameterizations are often regime-dependent, leading to models that artificially split the spectrum of atmospheric conditions into a discrete number of cases. Examples of such case-dependent approaches include parameterizations of cumulus (Arakawa, 2004) and stratocumulus clouds (Lilly, 1968; Schubert, 1976). However accurate, the use

of disparate schemes for different conditions complicates a seamless representation of subgrid-scale processes in the lower troposphere.

Several approaches to obtain a unified model of turbulence and convection have been proposed (Lappen & Randall, 2001; Park, 2014; Thuburn et al., 2018). Here we focus on the extended formulation of an eddy-diffusivity mass-flux (EDMF) scheme developed in Tan et al. (2018), which in turn built on work by Siebesma and Teixeira (2000); Soares et al. (2004); Siebesma et al. (2007) and Angevine et al. (2010), among others. In the EDMF framework, the flow within each grid cell is decomposed into several distinct subdomains, representing coherent convective structures and their relatively isotropic turbulent environment. Convective transport is captured by mass flux terms that depend on differences between subdomain-mean properties; more isotropic turbulent transport, associated with small-scale fluctuations within each subdomain, is captured by eddy diffusion closures.

The extended EDMF framework uses additional prognostic equations for subdomain variables, such as the environmental turbulence kinetic energy, and it requires closures for local turbulent fluxes and for the mass exchange between subdomains (Tan et al., 2018). Even though the EDMF framework arises from the need for a unified model of turbulence and convection, the parameterizations used for entrainment and turbulent mixing are usually defined differently for each regime (Suselj et al., 2013; Witek et al., 2011). The development of regime-independent parameterizations for the required closures is the last step in the construction of a unified model of atmospheric turbulence and convection.

Here, a regime-independent closure for turbulent mixing within the EDMF framework is proposed. Section 2 reviews the decomposition of subgrid-scale fluxes in the extended EDMF scheme. Section 3 introduces the formulation of the closure. Section 4 illustrates the performance of the EDMF scheme with the turbulent mixing closure in boundary layer regimes where vertical transport is strongly dependent on the turbulence closure used: the stable boundary layer (SBL), the stratocumulus-topped boundary layer (STBL), and dry convection. The performance of the extended EDMF scheme with this closure in moist-convective cases is demonstrated in a companion paper (Cohen et al., 2020). Finally, Section 5 summarizes the results and conclusions.

2 EDMF Framework

In the EDMF framework, each grid-cell volume is decomposed into n updrafts or downdrafts (labeled by index $i = 1, \ldots, n$) and an environment (labeled by index $i = 0$) in which they are embedded. Following this decomposition, the grid-mean value of variable ψ may be written as

$$\langle \psi \rangle = \sum_{i \geq 0}^{n} a_i \bar{\psi}_i. \tag{1}$$

Here, angle brackets $\langle \cdot \rangle$ denote the grid mean, $\bar{\psi}_i$ denotes the Favre average of ψ over subdomain i, and a_i is the mean horizontal cross-sectional area covered by subdomain i within the grid cell. This partition is motivated by the anisotropy of turbulent convective flows, in which isotropic turbulent eddies coexist with coherent columnar structures that induce a strong vertical transport (Bjerknes, 1938). The subdomain decomposition is simplified for the horizontal velocity $\mathbf{u}_h$, which is taken to have the same mean value for all subdomains, $\bar{\mathbf{u}}_{h,i} = \langle \mathbf{u}_h \rangle$. Applying the subdomain decomposition to higher-order moments introduces additional terms associated with the difference between grid and subdomain means. For the vertical subgrid-scale flux of ψ, this leads to

$$\langle w^* \psi^* \rangle = \sum_{i \geq 0}^{n} a_i \left(\overline{w_i' \psi_i'} + \bar{w}_i^* \bar{\psi}_i^* \right). \tag{2}$$

Here, w is the vertical velocity, $\psi^* = \psi - \langle\psi\rangle$, $\psi_i' = \psi - \bar{\psi}_i$, and $\bar{\psi}_i^* = \bar{\psi}_i - \langle\psi\rangle$. The decomposition (2) partitions the subgrid-scale flux into contributions from small-scale fluctuations, associated with turbulence, and subdomain-mean terms, representative of convection. In the following, we will refer to these contributions as turbulent and convective fluxes, respectively.

The subdomain-mean terms can be explicitly solved for by introducing n prognostic subdomain equations for each variable and an additional equation for each plume area fraction a_i, which may be diagnostic or prognostic (Tan et al., 2018). Turbulent fluxes within each subdomain are modeled as downgradient and proportional to an eddy diffusivity $K_{\psi,i}$, where ψ is the property being transported. For the vertical turbulent flux in (2), this gives

$$\overline{w_i'\psi_i'} = -K_{\psi,i}\frac{\partial\bar{\psi}_i}{\partial z}. \tag{3}$$

The eddy diffusivity $K_{\psi,i}$ is proportional to a characteristic velocity scale and the length scale of the eddies driving the transport, both of which must be parameterized.

Proposed closures for the eddy diffusivity vary from simple diagnostic expressions to second-order models that introduce prognostic equations for both scales (Umlauf & Burchard, 2003). The 1.5-order turbulence kinetic energy (TKE) model[1] is a particularly popular choice due to its balance between accuracy and computational efficiency (Mellor & Yamada, 1982). The 1.5-order model makes use of a prognostic equation for TKE and a diagnostic expression for the mixing length. In the EDMF framework, the grid-mean TKE $\langle e\rangle$ can be decomposed following expression (2) for second-order moments as

$$\langle e\rangle = \sum_{i\geq 0}^{n} a_i\left(\bar{e}_i + \frac{\bar{w}_i^*\bar{w}_i^*}{2}\right), \tag{4}$$

where $\bar{e}_i$ is the TKE of subdomain i. This expression can be simplified by assuming that for the updrafts and downdrafts ($i > 0$), the contribution to the grid-mean TKE from small-scale turbulence is negligible compared to the convective term, an assumption commonly made in EDMF schemes:

$$\langle e\rangle = a_0\bar{e}_0 + \sum_{i\geq 0}^{n} a_i\frac{\bar{w}_i^*\bar{w}_i^*}{2}. \tag{5}$$

The TKE decomposition (5) can also be obtained by assuming a small updraft and downdraft area fraction and similar turbulence intensity in all subdomains (Siebesma et al., 2007). However, the equations derived for the subdomain second-order moments with these two approaches differ in the source terms that appear due to entrainment processes between subdomains. The former approximation is favored here to allow for the use of this framework in high-resolution models, where the assumption of slender updrafts may become inadequate (Randall, 2013).

Given an updraft area fraction a_i, the grid-mean TKE is determined by the environmental TKE $\bar{e}_0$ and the subdomain-mean vertical velocities $\bar{w}_i$. The subdomain-mean vertical velocity equation for subdomain i is

$$\frac{\partial(\rho a_i\bar{w}_i)}{\partial t} + \frac{\partial(\rho a_i\bar{w}_i^2)}{\partial z} + \nabla_h\cdot(\rho a_i\bar{\mathbf{u}}_{h,i}\bar{w}_i) = -\frac{\partial(\rho a_i\overline{w_i'w_i'})}{\partial z} - \nabla_h\cdot(\rho a_i\overline{\mathbf{u}_{h,i}'w_i'}) + \sum_{j\neq i}\left[E_{ij}\bar{w}_j - \Delta_{ij}\bar{w}_i + \hat{E}_{ij}(\bar{w}_j - \bar{w}_i)\right] + \rho a_i\bar{b}_i - \rho a_i\frac{\partial\bar{\Psi}_i^\dagger}{\partial z}, \tag{6}$$

[1] This model is also referred to as the Level 2.5 model in the Mellor-Yamada hierarchy (Mellor & Yamada, 1982).

where ∇_h is the horizontal gradient operator, $\Psi = p/\rho$ is the pressure potential and the turbulent transport terms on the right-hand side are negligible for all subdomains except the environment ($i = 0$). Subgrid density changes are only considered in the buoyancy term, such that $\rho = \langle\rho\rangle$ in the previous equation, in order to avoid creation of spurious acoustic modes through the subdomain decomposition (Cohen et al., 2020). The buoyancy $\bar{b}_i$ and the pressure potential anomaly $\bar{\Psi}_i^\dagger$ are defined with respect to a reference hydrostatic pressure profile $p_h(z)$ and density $\rho_h(z)$, related by $\partial_z p_h = -\rho_h g$:

$$\bar{b}_i = -g\frac{\bar{\rho}_i - \rho_h}{\rho}, \qquad \frac{\partial\bar{\Psi}_i^\dagger}{\partial z} = \frac{\partial}{\partial z}\left(\frac{\bar{p}_i}{\rho}\right) + g\frac{\rho_h}{\rho}. \tag{7}$$

Here, $\bar{p}_i$ is the subdomain-mean pressure. Density appears inside the pressure gradients in (6) and (7) to ensure thermodynamic consistency of the subgrid-scale anelastic approximation (Cohen et al., 2020). Interactions between subdomains are captured by entrainment and detrainment fluxes. In the vertical velocity equation (6), Δ_{ij} is the dynamical detrainment of air mass from subdomain i into subdomain j, and E_{ij} and $\hat{E}_{ij}$ are the dynamical and turbulent entrainment from subdomain j into subdomain i, respectively. It is assumed that entrainment events occur over timescales much shorter than the eddy turnover rate $K_{\psi,i}/\bar{e}_i$, so that entrained air carries the properties of the subdomain it detrains from. In addition, for now we assume entrainment occurs only between convective plumes and the environment, not among plumes.

The prognostic equation for environmental TKE can be written in non-conservative form as

$$\begin{aligned}\frac{\partial\bar{e}_0}{\partial t} + \bar{w}_0\frac{\partial\bar{e}_0}{\partial z} + \langle\mathbf{u}_h\rangle\cdot\nabla_h\bar{e}_0 &= -\overline{w_0'u_0'}\frac{\partial\langle u\rangle}{\partial z} - \overline{w_0'v_0'}\frac{\partial\langle v\rangle}{\partial z} - \overline{w_0'^2}\frac{\partial\bar{w}_0}{\partial z} + \overline{w_0'b_0'} - \mathcal{P} \\ - \frac{1}{\rho a_0}\frac{\partial}{\partial z}\left(\rho a_0\overline{w_0'e_0'}\right) + \sum_{i>0}\left[\frac{\Delta_{i0}}{\rho a_0}\left(\frac{(\bar{w}_i - \bar{w}_0)^2}{2} - \bar{e}_0\right) - \frac{\hat{E}_{i0}}{\rho a_0}\left(\bar{w}_0^*(\bar{w}_i - \bar{w}_0) + \bar{e}_0\right)\right] - \mathcal{D} \\ - \frac{1}{\rho a_0}\nabla_h\cdot\left(\rho a_0\overline{\mathbf{u}_{h,0}'e_0'}\right) - \overline{\mathbf{u}_{h,0}'u_0'}\cdot\nabla_h\langle u\rangle - \overline{\mathbf{u}_{h,0}'v_0'}\cdot\nabla_h\langle v\rangle - \overline{\mathbf{u}_{h,0}'w_0'}\cdot\nabla_h\bar{w}_0.\end{aligned} \tag{8}$$

Here, $\langle u\rangle$ and $\langle v\rangle$ are the components of $\langle\mathbf{u}_h\rangle$, $\mathcal{P}$ is the velocity pressure-gradient correlation, and $\mathcal{D}$ is the turbulent dissipation. All sources and sinks of $\bar{e}_0$ account for unresolved processes on the grid scale, so they must be parameterized. Subdomain covariances in (8) are modeled diffusively, with the environmental eddy diffusivity K_ψ defined as

$$K_\psi = c_\psi l\bar{e}_0^{1/2}, \tag{9}$$

where l is the mixing length, and c_ψ is a fitting parameter. The subscript 0 in the eddy diffusivity is dropped to simplify notation. The coefficient c_ψ is taken to be equal to c_h for the diffusion of all fields except for momentum, for which $c_\psi = c_m$. The eddy viscosity K_m is related to K_h through the turbulent Prandtl number Pr_t, such that $K_m = \mathrm{Pr}_t K_h$.

Under the assumption that subgrid-scale pressure work on the grid-mean is negligible, $\mathcal{P}$ is taken as opposite to the pressure work on the plumes (Tan et al., 2018). Hence, $\mathcal{P}$ acts as a return-to-isotropy term on the full grid, transferring momentum from the strongly anisotropic coherent structures into the relatively isotropic eddies in the environment:

$$\mathcal{P} = \left[w_0'\left(\frac{\partial\Psi}{\partial z}\right)' + u_0'\left(\frac{\partial\Psi}{\partial x}\right)' + v_0'\left(\frac{\partial\Psi}{\partial y}\right)'\right]_0 = -\sum_{i>0}\frac{a_i}{a_0}(\bar{w}_i^* - \bar{w}_0^*)\frac{\partial\bar{\Psi}_i^*}{\partial z}, \tag{10}$$

The pressure work on the plumes is formulated in terms of contributions from a virtual mass term (Gregory, 2001), an advective term (Jia He, personal communication) and a

drag term (Romps & Charn, 2015), yielding the following expression for the velocity pressure-gradient correlation:

$$\mathcal{P} = -\sum_{i>0} \frac{a_i}{a_0}(\bar{w}_i^* - \bar{w}_0^*)\left(\alpha_b \bar{b}_i^* - \alpha_a \bar{w}_i^* \frac{\partial \bar{w}_i^*}{\partial z} + \alpha_d \frac{(\bar{w}_i^* - \bar{w}_0^*)|\bar{w}_i^* - \bar{w}_0^*|}{H_i}\right), \tag{11}$$

where α_a and α_d are constant parameters, H_i is the plume height and α_b is a function of the aspect ratio of the plume (Jia He, personal communication). Finally, assuming statistical equilibrium at scales l (Vassilicos, 2015), turbulent dissipation can be estimated from the spectral transport relation that follows from Kolmogorov's theory of inertial turbulence, giving Taylor's dissipation surrogate

$$\mathcal{D} = c_d \frac{\bar{e}_0^{3/2}}{l}. \tag{12}$$

Here, c_d is an empirical coefficient and l is the dissipation length, taken to be equal to the mixing length in our model. Expressions (3) and (5)–(12) provide closure to a 1.5-order model of turbulence within the EDMF framework, given diagnostic expressions for the mixing length l and for entrainment and detrainment.

3 Mixing Length Formulation

We seek to obtain a regime-independent eddy diffusivity closure that provides an accurate representation of turbulent subgrid-scale fluxes, over a wide range of host model resolutions. Thus, the eddy diffusivity should reduce to an LES-type closure at high resolution, while being able to account for the processes that modify turbulent fluxes at larger scales. The formulation of the closure is organized following this logic.

3.1 Minimum Dissipation of Environmental TKE

As in Verstappen (2011) and Abkar and Moin (2017), we assume that at the small scales represented by the environment in the EDMF scheme, TKE is dissipated at least at the rate at which it is produced. This condition translates into an inequality for the production and dissipation terms in the environmental TKE budget:

$$\begin{aligned}&\overline{w_0' b_0'} - \overline{w_0' u_0'}\frac{\partial \langle u\rangle}{\partial z} - \overline{w_0' v_0'}\frac{\partial \langle v\rangle}{\partial z} - \overline{w_0'^2}\frac{\partial \bar{w}_0}{\partial z} - \overline{\mathbf{u}_{h,0}' u_0'}\cdot\nabla_h\langle u\rangle - \overline{\mathbf{u}_{h,0}' v_0'}\cdot\nabla_h\langle v\rangle \\ &- \overline{\mathbf{u}_{h,0}' w_0'}\cdot\nabla_h \bar{w}_0 + \sum_{i>0}\left[\frac{\Delta_{i0}}{\rho a_0}\left(\frac{(\bar{w}_i - \bar{w}_0)^2}{2} - \bar{e}_0\right) - \frac{\hat{E}_{i0}}{\rho a_0}\left(\bar{w}_0^*(\bar{w}_i - \bar{w}_0) + \bar{e}_0\right)\right] \le \mathcal{D}. \end{aligned} \tag{13}$$

Here, the terms involving TKE injection from entrained air are also taken to be locally balanced by dissipation, consistent with the assumption that entrainment events occur over timescales much smaller than the eddy turnover time $K_{\psi,i}/\bar{e}_i$. The inequality (13) is a local condition for the environment, so it does not preclude net subgrid-scale energy production due to processes such as convection represented by plumes. The evolution of the grid-mean TKE that follows from (5) and (13) is

$$\begin{aligned}&\frac{\partial \langle e\rangle}{\partial t} + \langle \mathbf{u}_h\rangle\cdot\nabla_h\langle e\rangle + \langle w\rangle\frac{\partial \langle e\rangle}{\partial z} + \frac{\partial \langle w^* e^*\rangle}{\partial z} = \sum_i a_i\left(\bar{w}_i^*\bar{b}_i^* - \bar{w}_i^{*2}\frac{\partial \langle w\rangle}{\partial z}\right) - a_0\gamma_0 \\ &+ a_0\left(\overline{w_0' w_0'}\frac{\partial \bar{w}_0^*}{\partial z} + \overline{\mathbf{u}_{h,0}' w_0'}\cdot\nabla_h\bar{w}_0^*\right) - \sum_{i>0}\left[\frac{\Delta_{i0}}{\rho}\left(\frac{(\bar{w}_i - \bar{w}_0)^2}{2}\right) - \frac{\hat{E}_{i0}}{\rho}\bar{w}_0^*(\bar{w}_i - \bar{w}_0)\right], \end{aligned} \tag{14}$$

where γ_0 is the net environmental TKE dissipation with which the TKE production–dissipation inequality (13) becomes an equality. Under the net dissipation closure, grid-mean TKE production occurs through the first two terms on the right-hand side of (14): the convective buoyancy flux and the subdomain-scale shear production. The subgrid-scale kinetic energy pathways in the extended EDMF scheme are described in Appendix B.

Using Taylor's dissipation surrogate (12) and downgradient closures for the shear and buoyancy terms, the net dissipation condition (13) leads to a condition for the maximum value of the mixing length l at which the net dissipation γ_0 is still positive semidefinite:

$$\left\{\sum_{k=1}^{3}\left[\left(\frac{\partial\langle u\rangle}{\partial x_k}\right)^2+\left(\frac{\partial\langle v\rangle}{\partial x_k}\right)^2+\left(\frac{\partial\bar{w}_0}{\partial x_k}\right)^2\right]-\frac{1}{\mathrm{Pr}_t}\frac{\partial\bar{b}_0}{\partial z}\right\}l^2 + \sum_{i>0}\left[\frac{\Delta_{i0}}{\rho a_0}\left(\frac{(\bar{w}_i-\bar{w}_0)^2}{2}-\bar{e}_0\right)-\frac{\hat{E}_{i0}}{\rho a_0}\left(\bar{w}_0^*(\bar{w}_i-\bar{w}_0)+\bar{e}_0\right)\right]l\le\frac{c_d}{c_m}\bar{e}_0. \quad (15)$$

Here, the environmental buoyancy gradient is computed following Tan et al. (2018). From this inequality, an expression for the mixing length that minimizes turbulent dissipation can be obtained by solving for l. For the resulting value of the mixing length, production and dissipation of TKE are locally balanced:

$$l_{\mathrm{tke}}=\frac{\sqrt{\Delta}-\mathcal{I}}{2(\mathcal{S}_l+\mathcal{B}_l)}=-\frac{\mathcal{I}}{2(\mathcal{S}_l+\mathcal{B}_l)}+\frac{\sqrt{\mathcal{I}^2+4(\mathcal{S}+\mathcal{B})\mathcal{D}}}{2(\mathcal{S}_l+\mathcal{B}_l)}. \quad (16)$$

Here, Δ is the discriminant and the different terms are given by

$$\begin{aligned}\mathcal{S}_l+\mathcal{B}_l&=c_m\bar{e}_0^{1/2}\left\{\sum_{k=1}^{3}\left[\left(\frac{\partial\langle u\rangle}{\partial x_k}\right)^2+\left(\frac{\partial\langle v\rangle}{\partial x_k}\right)^2+\left(\frac{\partial\bar{w}_0}{\partial x_k}\right)^2\right]-\frac{1}{\mathrm{Pr}_t}\frac{\partial\bar{b}_0}{\partial z}\right\},\\ \mathcal{I}&=\sum_{i>0}\left[\frac{\Delta_{i0}}{\rho a_0}\left(\frac{(\bar{w}_i-\bar{w}_0)^2}{2}-\bar{e}_0\right)-\frac{\hat{E}_{i0}}{\rho a_0}\left(\bar{w}_0^*(\bar{w}_i-\bar{w}_0)+\bar{e}_0\right)\right],\\ \mathcal{S}+\mathcal{B}&=(\mathcal{S}_l+\mathcal{B}_l)l.\end{aligned} \quad (17)$$

In (16), the product $(\mathcal{S}+\mathcal{B})\mathcal{D}$ is independent of the mixing length, so l_{tke} can be readily evaluated. Although the term $(\mathcal{S}+\mathcal{B})$ is sign-indefinite, the discriminant

$$\Delta=\mathcal{I}^2+4(\mathcal{S}+\mathcal{B})\mathcal{D}$$

in (16) can be shown to remain positive semidefinite even when the shear and buoyancy terms result in TKE destruction, provided that the inequality (13) holds. This is because the minimum dissipation balance requires

$$\mathcal{I}=\mathcal{D}-(\mathcal{S}+\mathcal{B}), \quad (18)$$

so that the expression for the discriminant Δ is of the form

$$\Delta=[\mathcal{D}-(\mathcal{S}+\mathcal{B})]^2+4(\mathcal{S}+\mathcal{B})\mathcal{D}=[\mathcal{D}+(\mathcal{S}+\mathcal{B})]^2\ge 0. \quad (19)$$

The mixing length l_{tke} depends on local characteristics of the environment and on the vertical velocity difference between subdomains, which enter the entrainment and detrainment terms. Thus, convection modifies the environmental diffusive transport through entrainment processes. This approach can also be applied to turbulence models that retain covariance terms $\overline{w_i'\psi_i'}$ for other subdomains, and not only for the environment. In this case, the minimum dissipation condition may be used to obtain a characteristic mixing length $l_{\mathrm{tke},i}$ for each subdomain. However, variance within plumes can also be accounted for by variance among plumes when the number of subdomains is increased.

In stably stratified boundary layers, where convection is inhibited, pressure work and entrainment fluxes in (6) act to homogenize the different subdomains, such that $\bar{\psi}_i^*\to 0$ for any variable ψ and $a_0\to 1$ (i.e., there are no convective plumes). Under these conditions, the minimum dissipation mixing length (16) reduces to the expression proposed

by Grisogono (2010) for steady-state stable boundary layer (SBL) flow:

$$l_{\mathrm{tke}} = \frac{\sqrt{(\mathcal{S}+\mathcal{B})\mathcal{D}}}{(\mathcal{S}_l+\mathcal{B}_l)} = \sqrt{\frac{c_d}{c_m}\langle e\rangle}\left\{\sum_{k=1}^{3}\left[\left(\frac{\partial\langle u\rangle}{\partial x_k}\right)^2+\left(\frac{\partial\langle v\rangle}{\partial x_k}\right)^2+\left(\frac{\partial\langle w\rangle}{\partial x_k}\right)^2\right]-\frac{1}{\mathrm{Pr}_t}\frac{\partial\langle b\rangle}{\partial z}\right\}^{-1/2}. \quad (20)$$

The balance between shear production, destruction due to stratification, and dissipation, which arises when using this mixing length, is a well-known leading-order state in neutral (Spalart, 1988) and moderately stable boundary layer flows (Li et al., 2016).

3.2 Limitations of the Minimum-Dissipation Closure

Expression (16) for the mixing length l_{tke} captures the leading-order balance in the environmental TKE budget at small scales. However, a model with a diffusive closure based on l_{tke} cannot fully describe the dynamics of the boundary layer at the coarse resolutions typical of GCMs, on the order of 10^4 m in the horizontal and $10-100$ m in the vertical. At these scales, the resolved horizontal gradients are weak, and the environmental TKE equation (8) can be simplified using the boundary layer approximation (neglecting horizontal relative to vertical derivatives):

$$\frac{\partial\bar{e}_0}{\partial t}+\bar{w}_0\frac{\partial\bar{e}_0}{\partial z} = -\frac{1}{\rho a_0}\frac{\partial}{\partial z}\left(\rho a_0\overline{w_0'e_0'}\right)-\left(\overline{w_0'u_0'}\frac{\partial\langle u\rangle}{\partial z}+\overline{w_0'v_0'}\frac{\partial\langle v\rangle}{\partial z}+\overline{w_0'^2}\frac{\partial\bar{w}_0}{\partial z}\right)+\overline{w_0'b_0'} + \rho\sum_{i>0}\left[\frac{\Delta_{i0}}{\rho a_0}\left(\frac{(\bar{w}_i-\bar{w}_0)^2}{2}-\bar{e}_0\right)-\frac{\hat{E}_{i0}}{\rho a_0}\left(\bar{w}_0^*(\bar{w}_i-\bar{w}_0)+\bar{e}_0\right)\right]-\mathcal{P}-\mathcal{D}. \quad (21)$$

In stable conditions, using l_{tke} for the mixing length and integrating the conservative form of (21) from the surface layer (z_s) to the free troposphere above (z_i), the evolution equation for the vertically integrated environmental TKE reduces to

$$\int_{z_s}^{z_i}\frac{\partial(\rho a_0\bar{e}_0)}{\partial t}dz = -\left[\rho a_0\overline{w_0e_0}\right]_{z_s}^{z_i} \approx -\left.\rho a_0K_m\frac{\partial e_0}{\partial z}\right|_{z_s}. \quad (22)$$

Note that in stable conditions, $a_0 \approx 1$ and $\bar{\psi}_i^* \approx 0$ for any variable ψ. From (22), it follows that the evolution of the vertically integrated TKE under the minimum dissipation closure only depends on the flux from the unresolved surface layer. But unbalanced TKE dissipation has been observed to become increasingly important as stratification develops in field studies of the atmospheric boundary layer (Li et al., 2016), and it can be expected to play a role in conditions of strong surface cooling. The budget (22) cannot capture unbalanced TKE destruction within the boundary layer due to stratification. Furthermore, the minimum dissipation mixing length l_{tke} leads to enhanced eddy diffusion with increasing stratification, contrary to the evidence of turbulent mixing being inhibited in strong stratification, such as near strong inversions.

The limitations of a minimum dissipation model also become apparent in convectively unstable boundary layers. The use of expression (16) for the mixing length results in a simplified form of the TKE balance (21) because of the strict balance of all production and dissipation terms in (13). Integrating the TKE equation in the vertical, the evolution of the vertically integrated environmental TKE in convective conditions reads

$$\int_{z_s}^{z_i}\frac{\partial(\rho a_0\bar{e}_0)}{\partial t}dz = \rho a_0\overline{w_0\ e_0}|_{z_s}+\int_{z_s}^{z_i}\rho\sum_{i>0}a_i(\bar{w}_i^*-\bar{w}_0^*)\frac{\partial\bar{\Psi}_i^*}{\partial z}\,dz + \int_{z_s}^{z_i}\sum_{i>0}(\Delta_{i0}-E_{i0})\bar{e}_0\,dz. \quad (23)$$

Here, the last term only accounts for changes in environmental area fraction and does not result in a source or sink of $\bar{e}_0$. A major difference between the SBL budget (22) and the convective budget (23) is the contribution of the velocity pressure-gradient correlation. From the velocity pressure-gradient relation (11), pressure work captures the important energization of turbulence in the environment owing to ascending or descending plumes (Schumann & Moeng, 1991). At the grid-scale, the source of this subgrid-scale energy term is the convective buoyancy flux in (14), which accelerates the plumes in convective conditions.

The TKE balance (23) shows that, in convective conditions, the source of environmental TKE from updrafts or downdrafts can only be compensated by the flux from the unresolved surface layer. This is often a source term rather than a sink term, because shear production is surface intensified. Thus, the TKE balance (23) suggests an unbalanced growth of TKE in convective boundary layers. This continuous TKE increase in convective conditions is inconsistent with LES results showing quasi-stationary TKE levels in convective boundary layers (Nieuwstadt et al., 1993).

The TKE balances (22) and (23) highlight the shortcomings of the minimum dissipation balance (16) as a general closure for diffusive mixing in the boundary layer. The lack of net dissipation mechanisms in the vertically integrated TKE balance hinders the correct representation of important processes, such as the shallowing of the boundary layer in the late afternoon or the sharp mixing inhibition near inversions. Moreover, it precludes reaching a quasi-stationary state in statically unstable boundary layers. Nevertheless, the limitations of the minimum dissipation model can be used to inform the construction of a generalized master length scale based on the TKE production–dissipation inequality (13).

The limitations of the minimum dissipation balance showcased in this section are not necessarily applicable to other turbulence models. For example, He et al. (2019) use the production-dissipation condition to diagnose TKE and eddy diffusivity from a mixing length l. This allows an instantaneous adjustment of TKE to a new balanced state, at the cost of representing convection with an empirical parameterization that has no subgrid interaction with turbulent diffusion.

3.3 Constrained Minimization of TKE Dissipation

A master length scale that corrects the limitations of the minimum-dissipation model can be constructed by taking dissipation to be higher than production under certain circumstances. Using closures of the form (12) for the dissipation and (9) for turbulent diffusion, it follows from the production–dissipation inequality (13) that excess dissipation occurs for $l < l_{\mathrm{tke}}$. Hence, unbalanced TKE dissipation arises naturally in regions of the boundary layer where the characteristic size of environmental eddies is constrained to be smaller than l_{tke}. A general mixing length capturing this condition can be written as

$$l = s_{\min}(l_{\mathrm{tke}}, l_1, l_2, \ldots), \tag{24}$$

where l_j $(j = 1, 2, \ldots, N)$ are candidate mixing lengths based on flow constraints, and $s_{\min}(\mathbf{x})$ is a smooth minimum function defined in Appendix A. The TKE production–dissipation inequality (15) with the closures substituted implies that the minimum length scale provides maximum TKE dissipation. Thus, the use of the minimum length scale (24) is equivalent to the minimization of TKE dissipation in (13) subject to the constraint that dissipation exceeds the candidate dissipation rates,

$$\mathcal{D} \geq \mathcal{D}|_{l=l_j} \quad \forall j, \tag{25}$$

where $\mathcal{D}|_{l=l_j}$ is the candidate dissipation rate evaluated at length scale l_j.

Our suggestion for choosing a general mixing length as a smooth minimum of various candidates contrasts with the common practice (e.g., He et al., 2019; Han & Brether-

ton, 2019) to use the expression suggested by Blackadar (1962),

$$l_h = \left(\frac{1}{l_1} + \frac{1}{l_2} \right)^{-1}, \tag{26}$$

for a master length scale l_h. This length scale l_h, proportional to the harmonic mean of the candidates l_1 and l_2, is smaller than both l_1 and l_2. If closures similar to (9) and (12) are used in a prognostic equation for TKE, the mixing length (26) results in an unrealistic intensification of TKE dissipation in regions where the candidate length scales l_1 and l_2 are similar. This undesirable characteristic is avoided by using the smooth minimum (24).

We consider two limiting factors for the characteristic length scale of turbulent motion in boundary layer flows: stable stratification and the distance to solid boundaries.

3.3.1 Stratification Constraints

Environmental stratification constrains the size of turbulent eddies by inhibiting the vertical displacement of air masses. Stably stratified turbulence is known to show high vertical variability and reorganization into layered structures, with most mixing occurring within the layers (Waite, 2011). The thickness of these layers is determined by the vertical scale at which the governing dynamic equations become self-similar (Billant & Chomaz, 2001; Augier et al., 2012), known as the buoyancy scale l_b. For a flow with an imposed stratification given by the Brunt-Väisälä frequency N_e, this length scale is

$$l_b = c_b \frac{(\bar{e}_0)^{1/2}}{N_e}, \tag{27}$$

where c_b is an empirical coefficient. It is important to note that imposing l_b as an upper bound for the size of eddies is similar to doing so by the Ozmidov scale $l_o \sim \sqrt{\mathcal{D}/N_e^3}$ only if turbulent motions at the scale in question are assumed to be in the inertial subrange, such that (12) holds. In this case, an expression equivalent to (27) for the Ozmidov scale is

$$l_o = \left(\frac{c_b^3}{c_d} \frac{\mathcal{D}}{N_e^3} \right)^{1/2}. \tag{28}$$

However, recent experimental studies suggest that under strong stratification, turbulence may not display an inertial subrange (Grachev et al., 2013). In that case, expression (12) and the Ozmidov scale (28) may not be applicable (Li et al., 2016), whereas the buoyancy scale (27) still holds.

The buoyancy frequency of moist air depends on the latent heat release and evaporative cooling associated with the vertical displacement of air parcels. In general, the effective static stability N_e lies between the dry and the moist adiabatic limits. Following O'Gorman (2010), we use an effective static stability of the form

$$N_e^2 = \frac{g}{\bar{\theta}_{v,0}} \left(\frac{\partial \bar{\theta}_{v,0}}{\partial z} - \lambda \left. \frac{\partial \bar{\theta}_{v,0}}{\partial z} \right|_{\theta_{vl,0}} \right) = \frac{g}{\bar{\theta}_{v,0}} \left[(1-\lambda) \frac{\partial \bar{\theta}_{v,0}}{\partial z} + \lambda \frac{\partial \bar{\theta}_{v,0}}{\partial \bar{\theta}_{vl,0}} \frac{\partial \bar{\theta}_{vl,0}}{\partial z} \right], \tag{29}$$

where θ_v is the virtual potential temperature and λ represents the area fraction of environmental air undergoing phase change. In the non-precipitating cases considered here, λ is given by the environmental cloud fraction $f_{c,0}$. Cloud fraction diagnosis is cloud-type dependent in many current GCMs (Collins et al., 2004). In our EDMF scheme, we use a regime-independent probabilistic cloud scheme (see Appendix C). The liquid-water virtual potential temperature θ_{vl} appearing in the effective static stability measures the buoyancy of cloudy air parcels when moist-adiabatically returned to clear conditions,

$$\bar{\theta}_{vl} \approx (1 + \eta \bar{q}_t)\, \bar{\theta}_l \approx \bar{\theta}_v \exp\left(\frac{-L_v \bar{q}_l}{c_p \bar{T}} \right). \tag{30}$$

Here, $\eta = R_v/R_d - 1$, L_v is the latent heat of vaporization, c_p is the specific heat of air, q_t and q_l are the total and liquid water specific humidities, θ_l is the liquid water potential temperature, T is the temperature and R_v, R_d are the gas constants for water vapor and dry air, respectively. Note that the effective static stability (29) converges to the dry limit when $q_l \to 0$ for all values of λ; it reduces to $N_e^2 = (1-\lambda)N^2$, with dry buoyancy frequency N, in conditions that are well mixed in θ_l and q_t.

3.3.2 Wall Constraints

The presence of boundaries also imposes an upper limit on the size of eddies near them. Following Monin and Obukhov (1954), the eddy diffusivity in the surface layer has the form

$$K_{\psi,w} = \frac{u_* \kappa z}{\phi_\psi(\xi)} \tag{31}$$

where $\xi = z/L$, $\phi_\psi(\xi)$ is an empirical stability function, κ is the von Kármán constant, L is the Obukhov length, and u_* is the friction velocity. The upper bound for the mixing length near the surface is obtained by matching this eddy diffusivity with the expression (9) for the eddy diffusivity:

$$l_w = \frac{\kappa}{c_\psi \kappa_* \phi_\psi(\xi)} z. \tag{32}$$

Here, $\kappa_* = \bar{e}_0^{1/2}/u_*$ is the ratio of rms turbulent velocity to the friction velocity in the surface layer. The friction velocity in our model is diagnosed using the flux-profile relationships of Byun (1990), except in free convective conditions. When the conditions for free convection are satisfied, the diagnostic of u_*, which is a function of the horizontal wind speed at the lowest model level, is modified following Beljaars (1995).

The choice of a common master length for momentum and tracer diffusion implies $c_h \phi_h = c_m \phi_m$, such that $\phi_h = \mathrm{Pr}_t \phi_m$. In our formulation, the turbulent Prandtl number is taken to be a function of the gradient Richardson number Ri, based on a simplified cospectral budget of momentum and heat transport (Katul et al., 2013; Li, 2019):

$$\mathrm{Pr}_t = \frac{2\mathrm{Ri}}{1 + \omega_2 \mathrm{Ri} - \sqrt{-4\mathrm{Ri} + (1+\omega_2 \mathrm{Ri})^2}} \mathrm{Pr}_{t,0}. \tag{33}$$

Here, $\omega_2 = 40/13$ is a phenomenological constant, and $\mathrm{Pr}_{t,0}$ is the turbulent Prandtl number in neutral conditions. The stability function ϕ_m is often written in the form (Businger et al., 1971; Nakanishi, 2001)

$$\phi_m = [1 + a_1(\xi)\xi]^{a_2(\xi)}, \qquad a_i = a_i^- + (a_i^+ - a_i^-)H(\xi), \tag{34}$$

where $H(\cdot)$ is the Heaviside function and a_i^-, a_i^+ are empirical functions. The values of a_i^- are taken as negative definite to reflect the convective elongation of eddies in unstable conditions. In stable conditions, self-similarity of the flow requires that $a_2^+ = 1$ and $a_1^+ > 0$, such that under strong stratification, the mixing length (32) becomes independent of ξ. As shown by Monin and Obukhov (1954), the asymptotic limit of ϕ_m under strong stratification also requires that $a_1^+ = \mathrm{Pr}_t(\mathrm{Ri}_{\mathrm{st}})/\mathrm{Ri}_{\mathrm{st}}$. Here, $\mathrm{Ri}_{\mathrm{st}}$ is the asymptotic Richardson number at $\xi \gg 1/a_1^+$ in the surface layer.

The empirical function (34) has been shown to become increasingly inaccurate with stability for $\xi > 0.5$ (Sorbjan & Grachev, 2010; Optis et al., 2016). Moreover, extending the use of the limiting scale l_w above the surface layer precludes the use of $a_1^+ \neq 0$ in stable conditions, since the Obukhov length characterizes stratification only in the constant flux layer near the surface. Although the use of l_w in expression (24) mandates $a_1^+ = 0$, the effect of stability in eddy diffusion is still captured by l_b. In the constant flux layer, the limiting length l_b is equivalent to the use of the empirical function (34) in the strongly stable limit, with

$$a_1^+ = \frac{1}{(\kappa_*^2 c_m c_b)^2} \mathrm{Pr}_t, \qquad \xi \gg \frac{1}{a_1^+}. \tag{35}$$

Under weaker stratification, turbulence in the surface layer can reach a quasi-steady state (Spalart, 1988). In this case, the limiting scale l_w should converge to l_{tke}. Assuming that entrainment processes are limited to dynamical entrainment by the plumes in the surface layer, the ratio of the two length scales can be written as

$$\left.\frac{l_w}{l_{\text{tke}}}\right|_{\bar{e}_0} = \frac{(1 - \text{Ri}/\text{Pr}_t)^{1/2}}{(c_d c_m)^{1/2}\kappa_*^2}, \tag{36}$$

which is constant under neutral stratification and is slowly varying with Ri due to the opposing effect of the Prandtl number (33). From (36), the convergence of l_{tke} to l_w in the surface layer is satisfied for $(c_d c_m)^{1/2}\kappa_*^2 \approx 1$.

The use of a soft minimum function for the mixing length (24) allows for a smooth transition from Monin-Obukhov similarity theory near the surface to a local turbulent closure farther away from it, where the use of Monin-Obukhov scaling may be inaccurate (Optis et al., 2016). In addition, the expressions (35) and (36) show that this transition is asymptotically consistent.

3.3.3 Master Mixing Length

Finally, the smooth minimum of the three candidate length scales (16), (27), and (32) determines the mixing length,

$$l = s_{\min}(l_{\text{tke}}, l_w, l_b). \tag{37}$$

The mixing length (37) depends on a group of nondimensional parameters $\mathcal{C}$ that must be obtained empirically:

$$\mathcal{C} = \{c_m, c_d, c_b, \kappa, \kappa_*, a_1^-, a_2^-, \text{Pr}_{t,0}\}. \tag{38}$$

Values for these parameters are reported in studies of boundary layer turbulence, obtained from field observations (Businger et al., 1971) or LES (Nakanishi, 2001). However, the direct use of some of these values in the EDMF scheme is not justified due to the decomposition of the subgrid-scale flow into different subdomains. Because of the large size of the parameter space $\mathcal{C}$ and the presence of other parameters in the EDMF scheme, we limit the parameter optimization process to $\mathcal{C}^* = \{c_m, c_d, c_b\}$ in this study. $\mathcal{C}^*$ contains the parameters that appear in the closures that are most strongly affected by the domain decomposition. All other parameters in $\mathcal{C}$, except $\text{Pr}_{t,0}$, arise from similarity theory arguments for the unresolved surface layer. Here, it is assumed that similarity arguments are valid outside convective updrafts, and all values are taken from Nakanishi (2001). For the simulations reported in the next section, the parameter space used is shown in Table 1. The rest of parameters used in the EDMF scheme, which do not appear explicitly in the formulation of the mixing length closure, are reported in Cohen et al. (2020).

4 Results for Single-Column Simulations

Here we focus on case studies targeting the simulation of the Arctic stable boundary layer (SBL), stratocumulus clouds, and dry convection. The performance of the extended EDMF scheme in moist-convective cases is explored in Cohen et al. (2020), using the same set of parameters. The extended EDMF scheme is tested for horizontal resolutions typical of GCMs. Invoking the boundary layer approximation (neglecting horizontal derivatives), we perform simulations in a single-column model (SCM). The SCM is a one-dimensional vertical model that aims to represent a single atmospheric column within a GCM. Results from single-column simulations using the extended EDMF scheme are then compared to horizontal averages obtained from LES over the same domain. LES are set up by further discretizing the atmospheric column horizontally and using horizontal doubly-periodic boundary conditions.

Table 1. Parameters in the mixing length closure and values used in this study.

Symbol	Description	Value
c_m	Eddy viscosity coefficient	0.14
c_d	Turbulent dissipation coefficient	0.22
c_b	Static stability coefficient	0.63
κ	von Kármán constant	0.4
κ^*	Ratio of rms turbulent velocity to friction velocity	1.94
a_1^-	Empirical stability function coefficient	-100
a_2^-	Empirical stability function coefficient	-0.2
$\mathrm{Pr}_{t,0}$	Turbulent Prandtl number in neutral conditions	0.74

The EDMF scheme used here differs from the one described in Tan et al. (2018) in the parameterizations of the eddy diffusivity K_ψ, the vertical pressure anomaly gradients in (6) and (10), entrainment and detrainment, and the addition of turbulent entrainment $\hat{E}_{ij}$. The parameterization of the eddy diffusivity follows (9) and (37). The entrainment parameterization is described in Cohen et al. (2020), and the treatment of the pressure anomaly term is shown in (11). In addition, although the theoretical framework presented here allows for the use of downdrafts, the implementation used in this section decomposes the domain solely into one updraft and its turbulent environment.

LES are performed using PyCLES, an anelastic fluid solver in which the subgrid-scale fluxes are treated implicitly by the WENO scheme used to discretize the prognostic equations (Pressel et al., 2015). Implicit LES using WENO numerics have been shown to result in higher effective resolution than other combinations of numerics and explicit SGS closures (Pressel et al., 2017). Finally, LES results from previous model intercomparison projects are also reported where available.

4.1 Stable Boundary Layer

Statically stable conditions in the boundary layer inhibit convection, reducing the EDMF scheme to a diffusive closure. In the implementation of the scheme, this translates to conditioning the surface updraft area fraction on the sign of the surface buoyancy flux, such that it becomes zero in conditions of surface cooling. With no updrafts or downdrafts, the only contribution to the subgrid-scale flux (2) comes from the environmental downgradient turbulent flux (3). This leads to a high sensitivity of SCM simulations to changes in the mixing length formulation. Here we focus on the GEWEX Atmospheric Boundary Layer Study (GABLS), discussed in Beare et al. (2006).

4.1.1 Simulation Setup

The initial and boundary conditions of the simulation are adapted from observations during the Beaufort and Arctic Seas Experiment (Curry et al., 1997) and follow Beare et al. (2006). The velocity field is initialized as $(\langle u \rangle, \langle v \rangle) = (u_g, 0)$, where the geostrophic velocity is $u_g = 8$ ms^{-1}. The initial temperature sounding is given by a mixed layer with potential temperature $\theta = 265$ K up to 100 m, overlain by an inversion with a potential temperature gradient of 10 K km^{-1}. The surface boundary condition is given by constant cooling, $\dot{\theta}_{z=0} = -0.25$ K h^{-1}.

For both the SCM and LES, the domain height is 400 m. In the LES configuration, the domain spans 400 m in both horizontal directions as well. The LES data is generated using an isotropic mesh with $\Delta x_i = 3.125$ m resolution, which translates into $2{\times}10^6$ degrees of freedom. The full range of LES results from Beare et al. (2006), us-

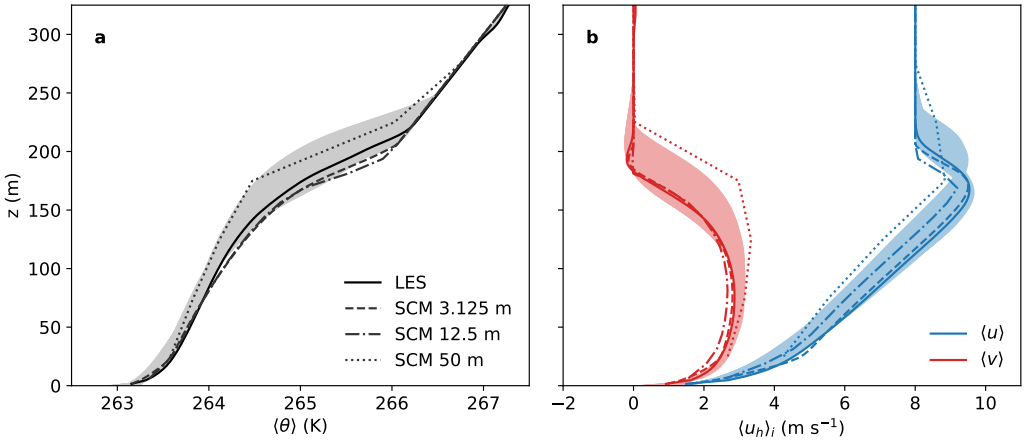

Figure 1. Profiles of (a) potential temperature and (b) horizontal velocity averaged over the ninth hour of the GABLS simulation. Results are shown for LES and for the EDMF-based SCM with $\Delta z = 3.125$ m, $\Delta z = 12.5$ m, and $\Delta z = 50$ m. The shaded region represents the spread of LES results with Δz=3.125 m reported in Beare et al. (2006).

ing the same resolution, is also included for reference. The SCM simulations are performed at vertical resolutions of $\Delta z = 3.125$ m, 12.5 m, and 50 m (128, 32, and 8 degrees of freedom, respectively). This range characterizes the performance of the EDMF scheme both at high resolution and for coarser resolutions typical of regional and global climate models in the lower troposphere.

4.1.2 Results

Figure 1 shows vertical profiles of $\langle\theta\rangle$, $\langle u\rangle$ and $\langle v\rangle$ time-averaged over the ninth hour of simulation. The EDMF scheme captures well the boundary layer height and the intensity of the low-level jet, with little resolution dependence of the mean profiles up to $\Delta z = 12.5$ m. At 50 m resolution, the SCM predicts a slightly deeper boundary layer. The EDMF-simulated TKE follows closely the LES data, as shown in Figure 2. The time-series show periods of TKE growth due to the subgrid momentum flux from the surface layer, and periods of decay due to the increasing stratification. These changes in vertically integrated TKE are much smaller than the integrated TKE production and dissipation terms, as shown in Figure 3. The domain-mean TKE budget, which coincides with the environmental budget for stable conditions, is shown in Figure 3.

The two main causes of grid-sensitivity at 50 m resolution are the inability to capture the region of maximum shear production close to the surface, and the deterioration of the friction velocity diagnosis. The effect of the former can be observed in Figure 3. Even if the budget is correctly captured above 50 m, the absence of grid-cells at the lower levels results in a significant reduction of the vertically integrated production and dissipation. In addition, the diagnosis of u_* based on Byun (1990) overestimates the friction velocity at coarser resolutions. This can be observed by comparing the normalized TKE profile to the vertically integrated timeseries in Figure 2.

The dominant mixing length throughout the simulation is shown in Figure 2 for all heights. Initially, the wall-limited mixing length l_w is dominant below the inversion, due to the absence of mean shear and stratification. As the shear and stratification develop, the dominant mixing length profile attains a three-layered structure. Closest to

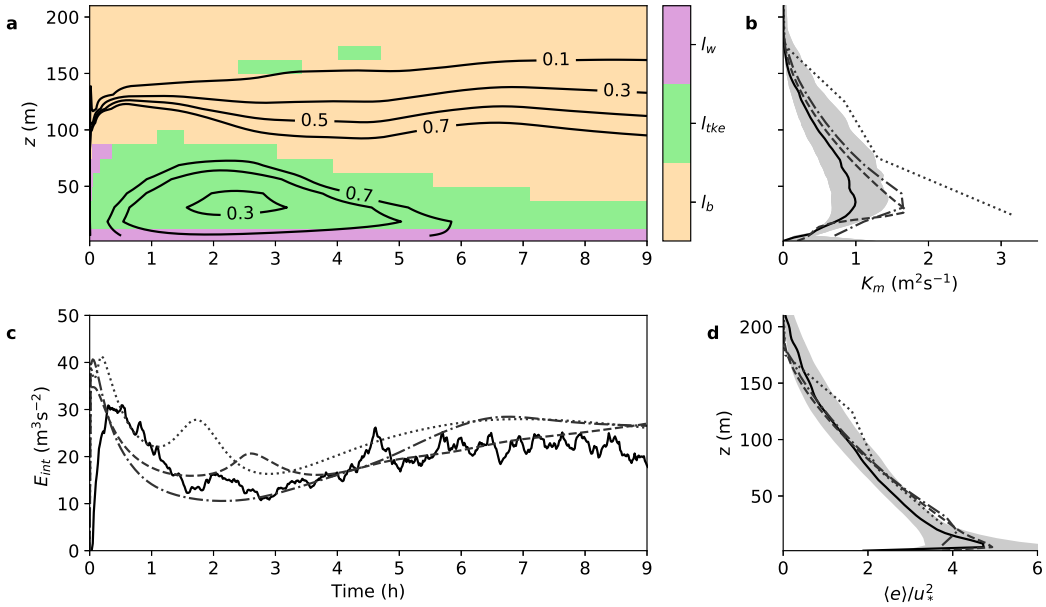

Figure 2. (a) Contours of eddy diffusivity K_m (m^2 s^{-1}) as a function of time and height for the GABLS simulation using the SCM with $\Delta z = 12.5$ m. Colors show the dominant (minimum) mixing length. (b) Profiles of eddy diffusivity averaged over the ninth hour. LES diffusivity is diagnosed from the shear production term $\mathcal{S}$ and the grid-mean shear. (c) Time series of vertically integrated TKE E_{int}. (d) Profiles of u_*-normalized TKE averaged over the ninth hour. In (b), (c) and (d), results are shown for LES (solid line), EDMF with $\Delta z = 3.125$ m (dashed line), $\Delta z = 12.5$ m (dash-dotted line), and $z = 50$ m (dotted line). The shaded region represents the spread of LES results with Δz=3.125 m reported in Beare et al. (2006).

the bottom boundary, the distance to the wall constrains the size of eddies. Farther away from the surface, the mixing length is determined by the local TKE balance. As stratification increases with height, the stratification-limited mixing length l_b becomes dominant, depleting TKE and limiting turbulent mixing. The eddy diffusivity, shown in Figure 2, is maximum near the transition from l_{tke} to l_b, where the mixing length is largest. Again, the overestimation of the friction velocity and the absence of grid-points in the lower layers result in an overestimation of the eddy diffusivity at coarse resolutions.

Both the LES and EDMF budgets show the quasi-balance of TKE sources and sinks throughout the boundary layer, even in regions where l_{tke} is not dominant. The downgradient parameterization of shear production $\mathcal{S}$, buoyant production $\mathcal{B}$, and the turbulent transport $\mathcal{T}$ results in profiles that follow closely the LES data, particularly at higher resolution. This validates the assumptions used to model the second-order moments in the extended EDMF scheme under stable stratification.

4.2 Stratocumulus-Topped Boundary Layer

The ability of the extended EDMF scheme to represent the dynamics of the STBL is tested using as a baseline the second Dynamics and Chemistry of Marine Stratocumulus (DYCOMS-II) field study (Stevens et al., 2003), performed near the coast of San Diego, California. In particular, the conditions observed during the first research flight (RF01) are considered, for which precipitation was not observed.

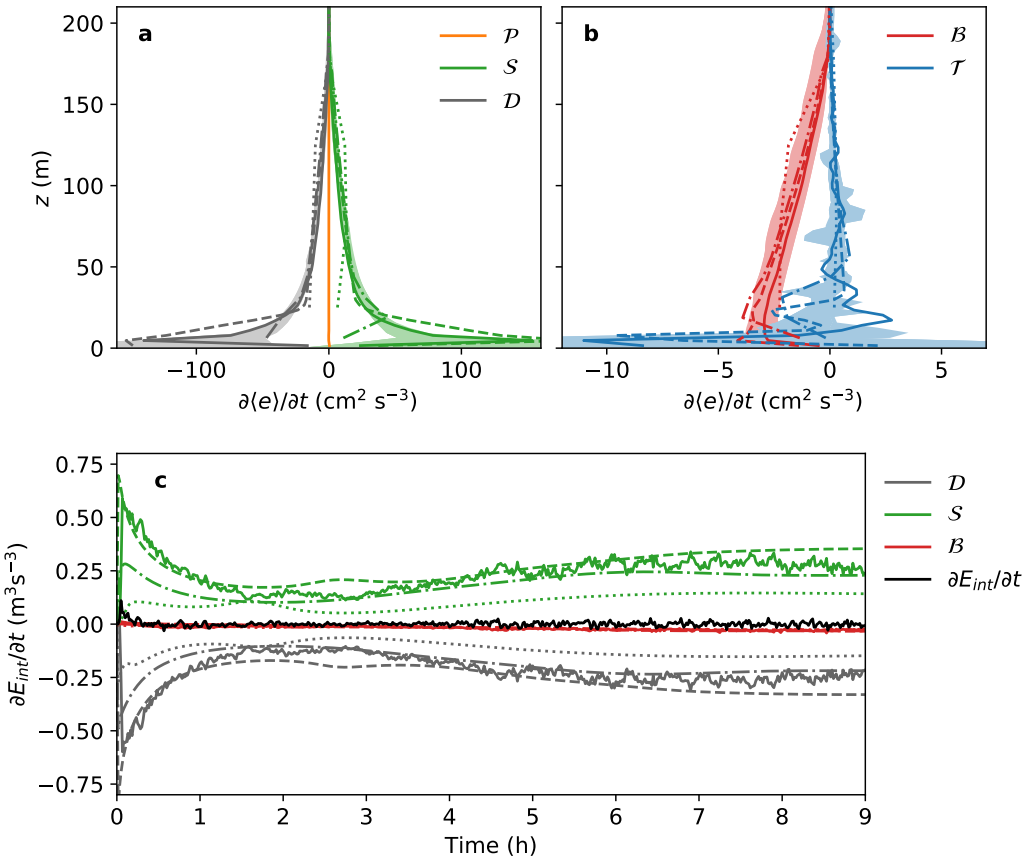

Figure 3. Profiles of TKE budget terms averaged over the ninth hour of GABLS simulation. Profiles shown in (a) are for shear production $\mathcal{S}$, dissipation $\mathcal{D}$ and the pressure term $\mathcal{P}$. Shown in (b) are the buoyant production term $\mathcal{B}$ and turbulent transport $\mathcal{T}$. (c) Time evolution of the vertically integrated TKE (E_{int}) production and dissipation terms. The rate of change of E_{int} in LES is included as a reference. Results are shown for LES (solid line) and for EDMF with $\Delta z = 3.125$ m (dashed line), $\Delta z = 12.5$ m (dash-dotted line), and $z = 50$ m (dotted line). The shaded region represents the spread of LES results with Δz=3.125 m reported in Beare et al. (2006).

4.2.1 Simulation Setup

The simulation setup for DYCOMS-II RF01 is reported in Stevens et al. (2005). The base state is initialized with a two-layer structure in θ_l and q_t, separated by a strong inversion at $z_i = 840$ m. The bottom layer is well-mixed in both conserved variables, with saturation and cloud formation occuring above 600 m. The cloud-top, located at z_i, is characterized by $\Delta\theta_l = 8.5$ K and $\Delta q_t = -7.5$ g kg^{-1}. The free troposphere is warmer and drier than the mixed layer, with a θ_l-lapse rate of $(1/3)(z-z_i)^{-2/3}$ K m^{-1} and constant q_t. The surface sensible and latent heat fluxes are set to 15 and 115 W m^{-2}, respectively. The vertical water distribution induces radiative cloud-base warming and radiative cooling at cloud-top and in the free troposphere.

The domain height is 1.5 km. In the LES, the horizontal domain extent is set to 3.36 km. The resolution used for the LES is $\Delta z = 5$ m in the vertical and $\Delta x = 35$ m in the horizontal. This corresponds to 2.76×10^6 degrees of freedom. The SCM simulations are performed with vertical resolutions of $\Delta z = 5$ m, $\Delta z = 20$ m and $\Delta z = 50$ m, or 300, 75, and 30 degrees of freedom, respectively.

4.2.2 Results

The mean profiles obtained with the extended EDMF scheme display very little resolution sensitivity compared to the spread of results from LES, as shown in Figure 4. LES of stratocumulus-topped boundary layers are strongly dependent on the discretization numerics and the treatment of subgrid-scale fluxes (Pressel et al., 2017). Overly diffusive LES models result in excessive cloud-top mixing, reducing the water content of the cloud layer and transitioning to decoupled cumulus-like conditions.

Similarly, the ability of SCM simulations to capture the stratocumulus-cloud layer is contingent upon the cloud-top mixing not being too strong. With large gradients in q_t and θ_l across the inversion, the mixing length is the main limiter of cloud-top diffusive mixing. As shown in Figure 5a, the buoyancy scale (27) is crucial to limit the cloud-top eddy diffusivity and maintain the sharp inversion. It is important to note that in our formulation, the mixing length may be smaller than Δz. This allows to maintain a coupled cloud layer even at 50 m vertical resolution.

How the dominant mixing length varies with height in the STBL is shown in Figure 5a. Throughout most of the boundary layer, environmental mixing is determined by the minimum-dissipation balance. Mixing is constrained by stratification at cloud top and in the lower part of the cloud, where the environmental cloud fraction $f_{c,0}$ is less than unity. The vertically integrated TKE obtained in the SCM simulations is similar across resolutions and follows closely the WENO-based LES statistics, as shown in Figure 5b. Again, the variation of TKE with resolution in the SCM simulations is significantly lower than the spread of values obtained with different LES, not all of which successfully simulate the presence of a stratocumulus cloud layer.

The liquid water path (LWP) time series from the SCM simulations are in agreement with the LES results. At coarse resolution, cloud-top entrainment of dry air is too low, which leads to an overestimation of q_l and LWP, as shown in Figures 4d and 5c. However, even at this resolution, the water content bias obtained with the EDMF scheme is significantly lower than the dry bias of some of the LES models.

The vertical heat and moisture fluxes, as well as the contributions from the turbulent flux (eddy diffusivity) and subdomain-mean terms (mass flux), are shown in Figure 4. The SCM simulations slightly overestimate the heat flux in the cloud layer and underestimate the moisture flux throughout the boundary layer. These biases compensate each other to some extent, leading to a small bias in the buoyancy flux. Similar bi-

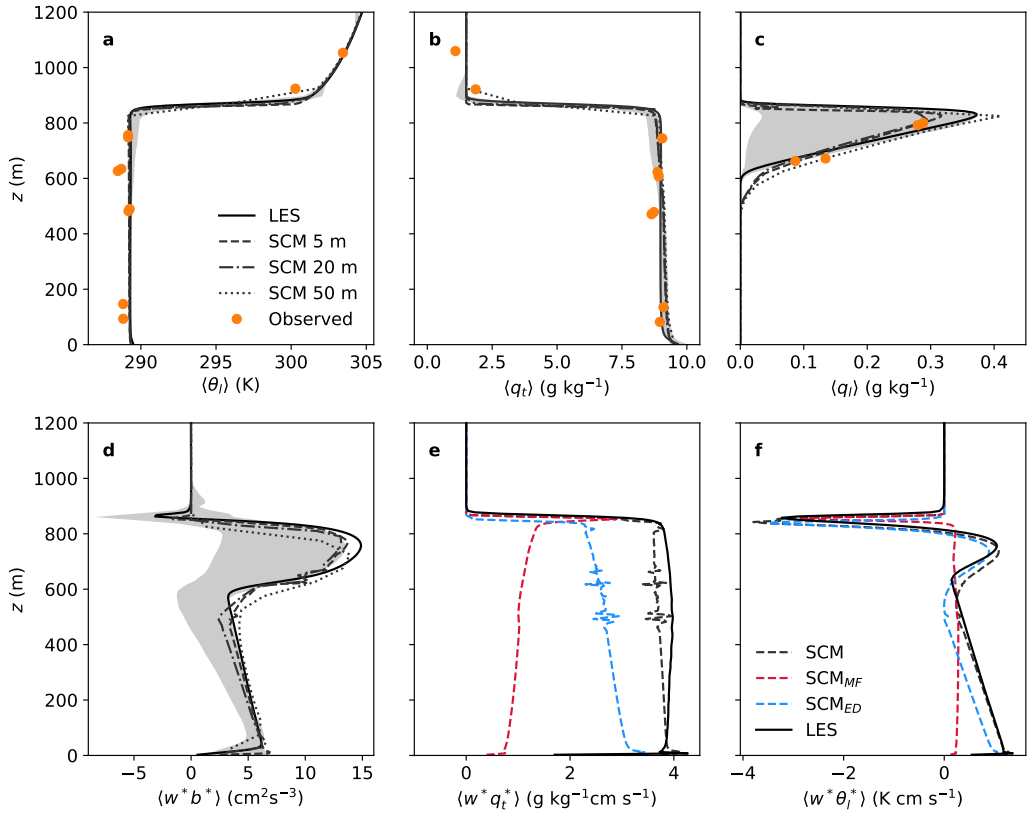

Figure 4. Profiles of (a) liquid water potential temperature, (b) total water specific humidity, (c) liquid water specific humidity, (d) vertical buoyancy flux, (e) vertical transport of q_t and (f) vertical transport of θ_l. Profiles averaged over the fourth hour of the DYCOMS-II RF01 simulation. In (e) and (f), the eddy diffusivity (SCM_{ED}) and mass flux (SCM_{MF}) components of the vertical flux are shown (plotting conventions follow the legend in panel (a)). The shaded region represents the spread of LES results reported in Stevens et al. (2005). Observations are also reported in Stevens et al. (2005).

ases are reported for models using the EDMF scheme and different parameterizations (Wu et al., 2020).

In the extended EDMF scheme, the environmental turbulent flux is the leading contributor to the buoyancy flux. The context of this decomposition should be considered when comparing these results to LES studies of the dynamics governing the STBL (e.g., Davini et al., 2017). Since we do not consider downdrafts in our SCM simulations, the environment contains all dynamic structures of the flow except updrafts. Therefore, the turbulent flux here also represents the transport due to downdrafts. Although LES studies emphasize the importance of convective transport due to downdrafts in stratocumulus clouds (Davini et al., 2017), we find that their implementation is not necessary to reproduce the STBL using the extended EDMF scheme. This is in agreement with Wu et al. (2020), where the authors show that the implementation of downdrafts in an EDMF scheme does not significantly improve simulations of the STBL.

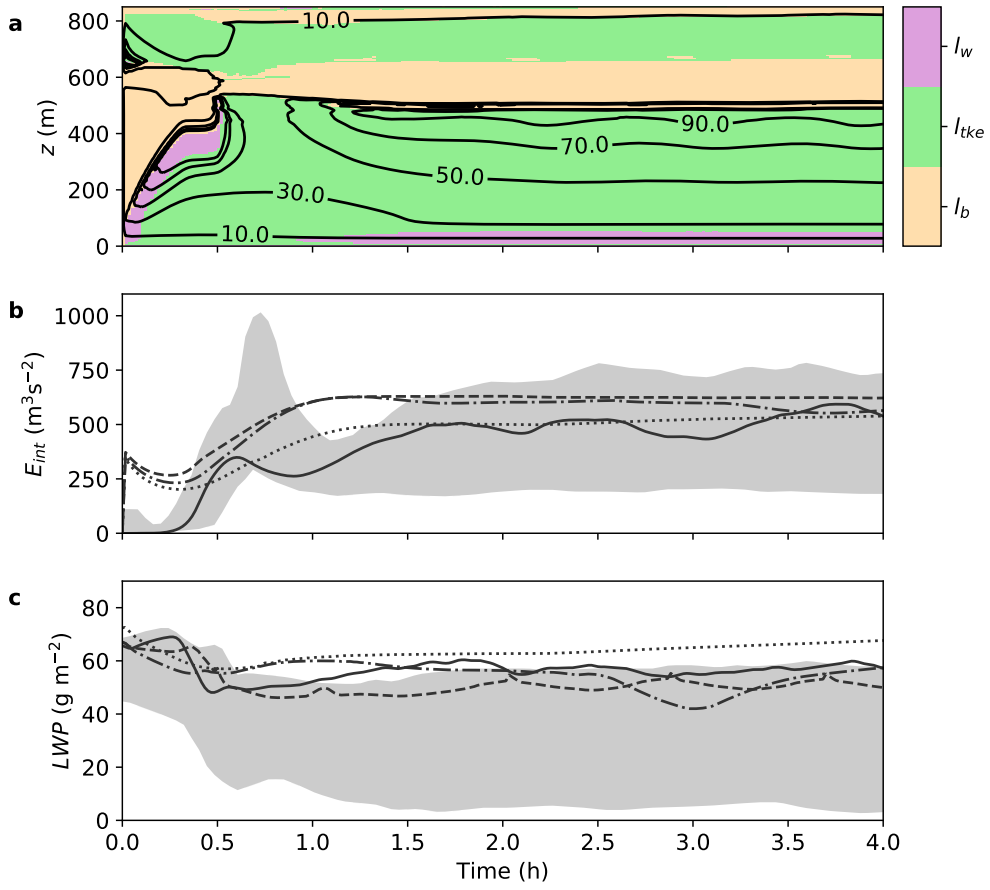

Figure 5. (a) Contours of eddy diffusivity K_m (m^2 s^{-1}) as a function of time and height for the DYCOMS-II RF01 simulation using the SCM with $\Delta z = 5$ m. Colors show the dominant (minimum) mixing length. (b) Time series of vertically integrated TKE E_{int}. (c) Time series of liquid water path (LWP). In (b) and (c), results are shown for LES (solid line), EDMF with $\Delta z = 5$ m (dashed line), $\Delta z = 20$ m (dash-dotted line), and $z = 50$ m (dotted line).

4.3 Dry Convection

The dry convective boundary layer differs from the previous cases in that the mass-flux term is the leading order contribution to the subgrid-scale vertical transport throughout most of the boundary layer. However, an accurate parameterization of the eddy-diffusivity contribution is still necessary for a correct simulation of the dry convective boundary layer.

4.3.1 Simulation Setup

The simulation setup follows Nieuwstadt et al. (1993). The flow is initialized from a mixed layer with potential temperature $\theta = 300$ K up to $z_1 = 1350$ m, above which potential temperature increases at a rate of 3 K km^{-1}. The flow, which is initialized with a horizontal velocity of 1 cm s^{-1}, is driven by a constant surface heat flux of $\langle w^*\theta^* \rangle = 6$ K cm s^{-1}.

The simulation is performed in a domain spanning 3.75 km in the vertical. For the LES, the horizontal cross-sectional area is 6.4×6.4 km^2, and the resolution is $\Delta z = 25$ m in the vertical and $\Delta x = 50$ m in the horizontal. The SCM simulations are performed with vertical resolutions of 25, 50, and 150 m.

4.3.2 Results

Time-averaged profiles of potential temperature and vertical buoyancy flux are shown in Figure 6. The potential temperature mixed layer and its associated vertical heat flux are well captured for all resolutions considered, with little resolution sensitivity. The convective heat flux is roughly constant throughout the boundary layer, while the diffusive flux decreases with height.

All simulations show a small cold bias throughout the boundary layer and a warm bias below the inversion. The latter is due to the absence of plume overshooting in the SCM simulations, as shown in Figure 6b. Reducing this bias with the extended EDMF scheme is possible, albeit with a different set of parameters controlling the pressure closure (11). These results are not shown here, since the goal of the model is to simulate all boundary layer regimes with a single set of parameters. Learning a set of parameters that minimizes this and other biases in the results shown here and in Cohen et al. (2020) is left for future work.

5 Summary and Discussion

The mixing length formulation proposed in this study provides a regime-independent closure of turbulent fluxes for EDMF schemes. The results for the stable boundary layer, stratocumulus-topped boundary layer, and dry convection demonstrate the ability of EDMF schemes with this mixing length closure to accurately describe the structure of the boundary layer in regimes where existing parameterizations currently in use in climate models fail or are inaccurate.

In the stable boundary layer, where convection and the subdomain decomposition in the EDMF scheme do not play a role, the proposed closure is able to reproduce the vertical structure and time evolution of turbulence over a range of vertical resolutions, down to $O(10$ m$)$. In the stratocumulus-topped boundary layer, where convective fluxes do play a role, the transport owing to environmental diffusion still provides the leading-order contribution to the subgrid-scale vertical fluxes in our EDMF scheme. The way in which environmental stratification limits the mixing length seems to be the crucial feature that allows our EDMF scheme to reproduce the sharp inversion at the stratocumulus cloud-top, even at relatively coarse vertical resolution.

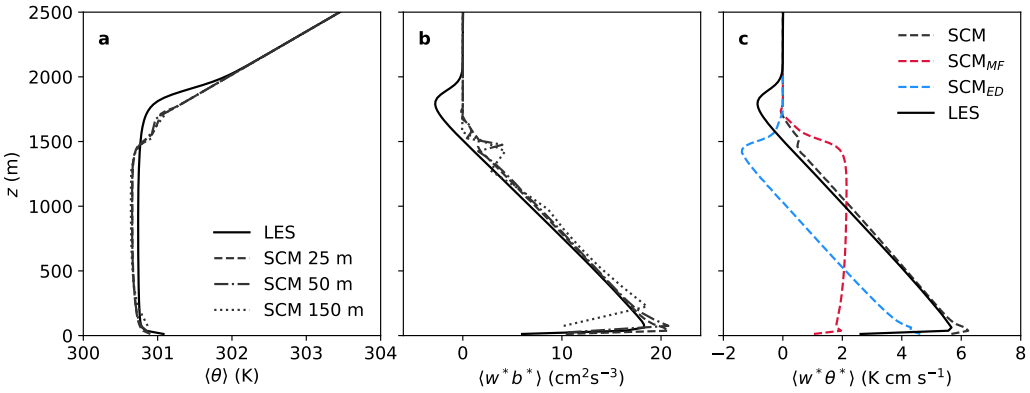

Figure 6. Profiles of (a) potential temperature, (b) vertical buoyancy flux, and (c) vertical transport of potential temperature. Profiles averaged over the fourth hour of simulation. In (c), the eddy diffusivity (SCM_{ED}) and mass flux (SCM_{MF}) components of the vertical flux are shown separately. Plotting conventions follow the legend in panel (a).

Several characteristics differentiate this closure from others proposed in the literature. First, choosing the smooth minimum (37) of various candidate mixing lengths is consistent with the idea that estimates of the mixing length arising from different physical arguments should converge to a similar master length scale if they are simultaneously valid. For widely used expressions such as (26), this does not hold, leading to unrealistic reductions in mixing. Second, our formulation explicitly links the eddy diffusivity to the effect of convective cells on the environment, leading to a consistently closed TKE balance. This results, for example, in the TKE injection term $\mathcal{I}$ appearing in the length scale (16), for which TKE production and dissipation are in balance. Third, the mixing length does not depend on integral quantities such as the boundary layer thickness or Deardorff's convective scale. The inclusion of these terms in other models often leads to regime-dependent nonlocal terms that are non-causal and hence difficult to justify in general. Finally, the closure smoothly connects with Monin-Obukhov similarity theory near the surface with no assumptions about the height at which the transition occurs. This is particularly relevant for low-resolution climate models, for which the use of similarity theory even in the first model level may be inaccurate.

A similar approach to the one shown here may be used to develop increasingly complex closures for high-order turbulence models. As an example, the net dissipation argument used in the TKE production–dissipation inequality (13) can also be applied to the temperature variance budget to diagnose the turbulent Prandtl number. The same could be done for other second-moment budgets in models with additional second-order prognostic equations, to obtain independent diffusivities for different tracers.

Finally, the optimization of the full parameter space was beyond the scope of this study and is left for future work. The access to LES data for a wider range of atmospheric conditions is necessary to enable a more comprehensive optimization of the parameter space in the EDMF scheme.

Appendix A Smooth Minimum Function

We define as a smooth minimum any function $f : R^N \to R$ of differentiability class C^∞ that approximates the $\min(\mathbf{x})$ operator. Our implementation of (37) is based on the softmin function $\mathbf{s}^\Lambda(\mathbf{x})$, which is a smooth approximation to the $\mathrm{argmin}(\mathbf{x})$ func-

tion (Titsias, 2016), with

$$s_j^\Lambda(\mathbf{x}) = \frac{e^{-x_j/\Lambda}}{\sum_{i=1}^N e^{-x_i/\Lambda}}. \tag{A1}$$

Here, Λ is a regularization parameter. The inner product of $\mathbf{s}^\Lambda$ with $\mathbf{x}$ yields an approximation of the $\min(\mathbf{x})$ operator,

$$\sigma^\Lambda(\mathbf{x}) = \mathbf{x}\cdot\mathbf{s}^\Lambda(\tilde{\mathbf{x}}) = \frac{\sum_{i=1}^N x_j e^{-\tilde{x}_j/\Lambda}}{\sum_{i=1}^N e^{-\tilde{x}_i/\Lambda}}, \tag{A2}$$

where $\tilde{x}_j = x_j - \min(\mathbf{x})$. In (A2), the translational symmetry $\mathbf{s}^\Lambda(\mathbf{x}) = \mathbf{s}^\Lambda(\mathbf{x}+\mathbf{c})$ with $c_j = c$ is used to avoid errors due to finite precision arithmetic. The function $\sigma^\Lambda(\mathbf{x})$ converges to $\min(\mathbf{x})$ as $\Lambda \to 0$. In practice, a nonzero regularization parameter is chosen to ensure smoothness. The value of Λ may be obtained by imposing a monotonically decreasing contribution of each x_j to $\sigma^\Lambda(\mathbf{x})$:

$$\frac{\partial\left(x_j s_j^\Lambda(\mathbf{x})\right)}{\partial x_j} \le 0 \quad \forall x_j \quad \text{if} \quad \Lambda \le \min(\mathbf{x}). \tag{A3}$$

Alternatively, Λ may be defined by enforcing an upper bound on the value of $\sigma^\Lambda(\mathbf{x})$ under certain assumptions about $\mathbf{x}$. Let the elements of $\mathbf{x}$ be ordered such that $x_j \le x_{j+1}$ for all j. Assuming $x_2 \approx x_n \ll x_{n+1}$, then

$$\sigma^\Lambda(\mathbf{x}) \le \min(\mathbf{x})(1+\epsilon) \quad \text{if} \quad \Lambda \le \Lambda_0 = \frac{\epsilon}{W(\frac{n-1}{e})}\min(\mathbf{x}), \tag{A4}$$

where $W(x)$ is the Lambert W function. In the implementation of (37), we use

$$s_{\min}(\mathbf{x}) = \sigma^{\Lambda_0^*}(\mathbf{x}) \quad \text{with} \quad \epsilon = 0.1. \tag{A5}$$

Here, $\Lambda_0^* = \max(\Lambda_0, 1.0\text{ m})$, so the smoothing scale is constrained to be at least 1 m. Although a large value of n results in a closer approximation to the minimum, (A1) may become difficult to evaluate in finite precision arithmetic. Because of the low dimensionality of $\mathbf{x}$ in (37) and the limitation given by Λ_0^*, finding a compromise is not necessary, and we set $n = N$.

Appendix B Subgrid Kinetic Energy in the Extended EDMF Scheme

According to the TKE decomposition (5), the grid-mean TKE includes the environmental TKE and the subgrid kinetic energy of the plumes. The environmental TKE equation in flux form reads

$$\begin{aligned}
&\frac{\partial(\rho a_0 \bar{e}_0)}{\partial t} + \nabla_h\cdot(\rho a_0\langle\mathbf{u}_h\rangle\bar{e}_0) + \frac{\partial(\rho a_0\bar{w}_0\bar{e}_0)}{\partial z} = -\frac{\partial(\rho a_0\overline{w_0'e_0'})}{\partial z} + \rho a_0\overline{w_0'b_0'} \\
&\quad - \rho a_0\left[\overline{w_0'u_0'}\frac{\partial\langle u\rangle}{\partial z} - \overline{w_0'v_0'}\frac{\partial\langle v\rangle}{\partial z} - \overline{w_0'w_0'}\frac{\partial\bar{w}_0}{\partial z}\right] + \rho\sum_{i>0} a_i(\bar{w}_i^* - \bar{w}_0^*)\frac{\partial\bar{\Psi}_i^*}{\partial z} \\
&\quad + \sum_j\left[E_{0j}\frac{1}{2}(\bar{w}_j - \bar{w}_0)^2 - (\Delta_{0j} + \hat{E}_{0j})\bar{e}_0 - \hat{E}_{0j}\bar{w}_0^*(\bar{w}_j^* - \bar{w}_0^*)\right] - \rho a_0\mathcal{D} \\
&- \nabla_h\cdot\left(\rho a_0\overline{\mathbf{u}_{h,0}'e_0'}\right) - \rho a_0\left(\overline{\mathbf{u}_{h,0}'u_0'}\cdot\nabla_h\langle u\rangle - \overline{\mathbf{u}_{h,0}'v_0'}\cdot\nabla_h\langle v\rangle - \overline{\mathbf{u}_{h,0}'w_0'}\cdot\nabla_h\bar{w}_0\right).
\end{aligned} \tag{B1}$$

The prognostic equation for the convective kinetic energy in subdomain i can be obtained as

$$\frac{1}{2}\frac{\partial\rho a_i\bar{w}_i^{*2}}{\partial t} = \bar{w}_i^*\left[\frac{\partial\rho a_i\bar{w}_i}{\partial t} - a_i\frac{\partial\rho\langle w\rangle}{\partial t} - \langle w\rangle\frac{\partial\rho a_i}{\partial t} + a_i\langle w\rangle\frac{\partial\rho}{\partial t} + \frac{\bar{w}_i^*}{2}\frac{\partial\rho a_i}{\partial t}\right]. \tag{B2}$$

Summing over all subdomains, we obtain the subgrid-scale convective TKE balance

$$\begin{aligned}\frac{1}{2}\sum_i\Big[\frac{\partial\rho a_i\bar{w}_i^{*2}}{\partial t}+\nabla_h\cdot\left(\rho a_i\langle\mathbf{u}_h\rangle\bar{w}_i^{*2}\right)+\frac{\partial\left(\rho a_i\bar{w}_i\bar{w}_i^{*2}\right)}{\partial z}\Big]&=-\sum_i\frac{\partial(\rho a_i\bar{w}_i^*\overline{w_i'w_i'})}{\partial z}\\&+\sum_i\Big(-\rho a_i\bar{w}_i^{*2}\frac{\partial\langle w\rangle}{\partial z}+\rho a_i\overline{w_i'w_i'}\frac{\partial\bar{w}_i^*}{\partial z}+\rho a_i\bar{b}_i^*\bar{w}_i^*-\rho a_i\frac{\partial\bar{\Psi}_i^*}{\partial z}\bar{w}_i^*\Big)\\&+\sum_i\Big[\rho a_i\overline{\mathbf{u}_{h,i}'w_i'}\cdot\nabla_h\bar{w}_i^*-\nabla_h\cdot(\rho a_i\bar{w}_i^*\overline{\mathbf{u}_{h,i}'w_i'})\Big]\\&-\sum_i\sum_{j\neq i}\Big[E_{ij}\frac{(\bar{w}_j^*-\bar{w}_i^*)^2}{2}-\hat{E}_{ij}\bar{w}_i^*(\bar{w}_j^*-\bar{w}_i^*)\Big].\end{aligned}\tag{B3}$$

The divergence terms on the right-hand side are turbulent transport terms. The second term represents shear production of convective energy. The third one yields shear production of TKE by the convective flow, which represents an advective sink in the balance (B3). The fourth and fifth terms are the convective components of the buoyant production and velocity-pressure gradient terms. The dynamical and turbulent entrainment terms act to transfer subgrid kinetic energy from the plumes to within-subdomain variance. Finally, all terms involving within-subdomain covariances are only nonzero in the environment, under the EDMF assumptions.

Some of the terms in budgets (B1) and (B3) transfer subgrid energy among the environment and plumes, resulting in a null contribution to the global budget. The grid-mean TKE prognostic equation that results from their sum is

$$\begin{aligned}\frac{\partial(\rho\langle e\rangle)}{\partial t}+\nabla_h\cdot(\rho\langle\mathbf{u}_h e\rangle)+\frac{\partial(\rho\langle we\rangle)}{\partial z}&=\rho\langle w^*b^*\rangle-\sum_{k=1}^{3}\rho\left\langle u_k^*\frac{\partial\Psi^*}{\partial x_k}\right\rangle-\rho a_0\mathcal{D}\\&-\rho\Big(\langle w^*u^*\rangle\frac{\partial\langle u\rangle}{\partial z}+\langle w^*v^*\rangle\frac{\partial\langle v\rangle}{\partial z}+\langle w^*w^*\rangle\frac{\partial\langle w\rangle}{\partial z}\Big)\\&-\rho\Big(\langle\mathbf{u}_h{}^*u^*\rangle\cdot\nabla_h\langle u\rangle+\langle\mathbf{u}_h{}^*v^*\rangle\cdot\nabla_h\langle v\rangle+\langle\mathbf{u}_h{}^*w^*\rangle\cdot\nabla_h\langle w\rangle\Big),\end{aligned}\tag{B4}$$

where the pressure term has no contribution in our model. The evolution of the grid-mean TKE under the net dissipation closure can be obtained by subtracting (13) from (B4):

$$\begin{aligned}\frac{\partial(\rho\langle e\rangle)}{\partial t}+\nabla_h\cdot(\rho\langle\mathbf{u}_h e\rangle)+\frac{\partial(\rho\langle we\rangle)}{\partial z}&=\underbrace{\sum_i\rho a_i\bar{b}_i^*\bar{w}_i^*}_{\mathcal{B}^*}\underbrace{-\sum_i\rho a_i\bar{w}_i^{*2}\frac{\partial\langle w\rangle}{\partial z}}_{\mathcal{S}^*}-\rho a_0\gamma_0\\&+\underbrace{\sum_i\rho a_i\left[\overline{w_i'^2}\cdot\frac{\partial\bar{w}_i^*}{\partial z}+\overline{\mathbf{u}_{h,i}'w_i'}\cdot\nabla_h\bar{w}_i^*\right]}_{\text{Advective sink}}\underbrace{-\sum_i\sum_{j\neq i}\Big[E_{ij}\frac{(\bar{w}_j^*-\bar{w}_i^*)^2}{2}-\hat{E}_{ij}\bar{w}_i^*(\bar{w}_j^*-\bar{w}_i^*)\Big]}_{\text{Turb. and dyn. entrainment}},\end{aligned}\tag{B5}$$

where γ_0 is the net environmental dissipation. According to (B5), grid-mean TKE is generated through convective buoyant production $\mathcal{B}^*$ and the vertical convergence term $\mathcal{S}^*$. Both dynamical and turbulent entrainment act as a transfer term from subgrid-scale convective kinetic energy to environmental TKE, resulting in a grid-mean TKE sink under the net dissipation closure. A schematic of the energetic pathways between budgets (B1) and (B3) and the overall evolution of grid-mean TKE under the mixing length closure presented here is shown in Figure B1.

Appendix C Probabilistic Model for Cloud Fraction

We consider θ_l and q_t to be log-normally distributed with expected values $\bar{\theta}_{l,0}$ and $\bar{q}_{t,0}$, variances $\sigma^2_{\theta_l}$ and $\sigma^2_{q_t}$, and covariance $\sigma^2_{q_t,\theta_l}$.The log-normal distribution is preferred

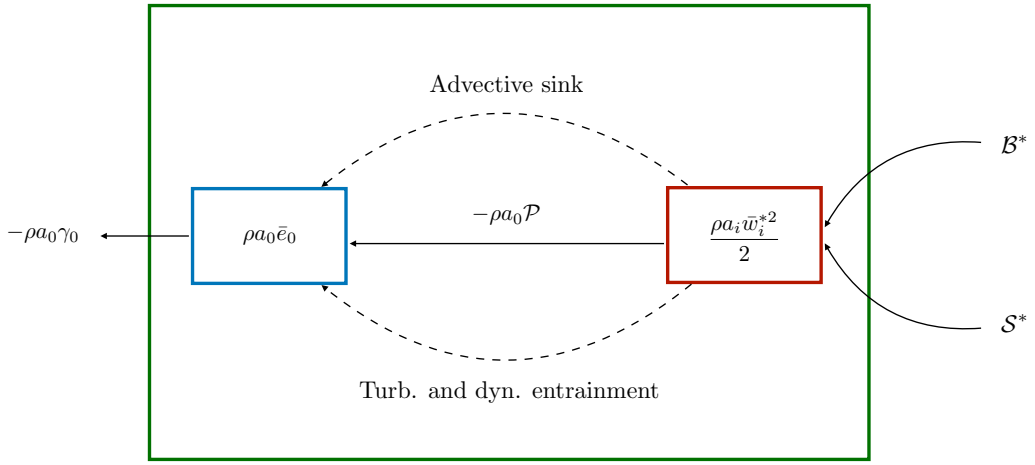

Figure B1. Schematic of subgrid kinetic energy reservoirs and pathways in the extended EDMF scheme under the net dissipation closure. Notation follows equation (B5). Dashed lines represent energy pathways that result in implicit grid-mean TKE dissipation under the net dissipation closure (13). Summation over $i = 0, \ldots, n$ is implied.

over the commonly used Gaussian distribution (e.g., Sommeria & Deardorff, 1977) for two reasons: both θ_l and q_t remain non-negative, and positive skewness is allowed. Under the Gaussian assumption, negative values of q_t may be drawn from the distribution if $\sigma_{q_t}^2/\bar{q}_{t,0}^2$ is not sufficiently small (Mellor, 1977). In addition, distributions with positive skewness have been shown to capture the development of cumulus convection better (Bougeault, 1981).

The expected value of cloud fraction $f_{c,0}$ can be computed as (Mellor, 1977)

$$f_{c,0} = \int_{-\infty}^{\infty} \int_{-\infty}^{\infty} H(q_l(\theta_l, q_t)) p(\theta_l, q_t)\, d\theta_l\, dq_t, \tag{C1}$$

where $H(\cdot)$ is the Heaviside function and $p(\theta_l, q_t)$ is the probability density function (PDF) of the log-normal bivariate distribution with marginal probability density functions (PDFs) given by

$$q_t \sim \mathrm{LN}(\mu_{q_t}, s_{q_t}^2), \qquad \mu_{q_t} = \ln\left(\frac{\bar{q}_{t,0}^2}{\sqrt{\sigma_{q_t}^2 + \bar{q}_{t,0}^2}}\right), \qquad s_{q_t}^2 = \ln\left(\frac{\sigma_{q_t}^2}{\bar{q}_{t,0}^2} + 1\right) \tag{C2}$$

and

$$\theta_l \sim \mathrm{LN}(\mu_{\theta_l}, s_{\theta_l}^2), \qquad \mu_{\theta_l} = \ln\left(\frac{\bar{\theta}_{l,0}^2}{\sqrt{\sigma_{\theta_l}^2 + \bar{\theta}_{l,0}^2}}\right), \qquad s_{\theta_l}^2 = \ln\left(\frac{\sigma_{\theta_l}^2}{\bar{\theta}_{l,0}^2} + 1\right). \tag{C3}$$

The conditional PDF of θ_l given q_t is the log-normal distribution

$$\theta_l | q_t \sim \mathrm{LN}(\mu_c, s_c^2), \qquad \mu_c = \mu_{\theta_l} + \frac{s_{\theta_l,q_t}^2}{s_{q_t}^2}(\ln(q_t) - \mu_{q_t}), \qquad s_c^2 = s_{\theta_l}^2 - \frac{s_{\theta_l,q_t}^4}{s_{q_t}^2}, \tag{C4}$$

where

$$s_{\theta_l,q_t}^2 = \ln\left(\frac{\sigma_{q_t,\theta_l}^2}{\bar{q}_{t,0}\bar{\theta}_{l,0}} + 1\right). \tag{C5}$$

The cloud fraction (C1) can be calculated by Gaussian quadrature as

$$f_{c,0} \approx \frac{1}{\pi} \sum_{i}^{n_i} w_i \sum_{j}^{n_j} w_j H(q_l(\theta_{l,j}, q_{t,i})), \tag{C6}$$

where w_j and w_i are the Gauss-Hermite weights corresponding to evaluation points $\theta_{l,j}$ and $q_{t,i}$, respectively. The evaluation points $(\theta_{l,j}, q_{t,i})$ of the log-normal distributions (C2) and (C4) are related to the Gauss-Hermite mass points (ξ_j, χ_i) through the normal distributions x and y with same parameters:

$$\theta_{l,j} = e^{x_j}, \qquad x_j = \mu_c + \sqrt{2} s_c \xi_j, \qquad x \sim N(\mu_c, s_c^2) \tag{C7}$$

and

$$q_{t,i} = e^{y_i}, \qquad y_i = \mu_{q_t} + \sqrt{2} s_{q_t} \chi_i, \qquad y \sim N(\mu_{q_t}, s_{q_t}^2). \tag{C8}$$

Note that the evaluation points $\theta_{l,j}$ are drawn from the conditional PDF (C4). In (C6), the liquid water specific humidity q_l is obtained as $q_l = q_{t,i} - q_s(\theta_{l,j}, q_{t,i})$, where q_s is the equilibrium saturation specific humidity. Thus, supersaturation is not considered and all excess water vapour is immediately converted to liquid water condensate. The equilibrium saturation specific humidity is found iteratively using a saturation adjustment procedure (see Bryan & Fritsch, 2002, for details). Consistent with this approach, the environmental liquid water specific humidity $\bar{q}_{l,0}$ is computed as

$$\bar{q}_{l,0} = \frac{1}{\pi} \sum_{i}^{n_i} w_i \sum_{j}^{n_j} w_j [q_{t,i} - q_s(\theta_{l,j}, q_{t,i})]. \tag{C9}$$

In this study, the probabilistic cloud model is implemented using $n_i = n_j = 3$.

Acknowledgments

This research was made possible by the generosity of Eric and Wendy Schmidt by recommendation of the Schmidt Futures program, by Earthrise Alliance, Mountain Philanthropies, the Paul G. Allen Family Foundation, and the National Science Foundation (NSF, award AGS-1835860). I.L. was additionally supported by a Resnick Sustainability Fellowship. Parts of the research were carried out at the Jet Propulsion Laboratory, California Institute of Technology, under a contract with the National Aeronautics and Space Administration and funded through the internal Research and Technology Development program.

References

Abkar, M., & Moin, P. (2017). Large-eddy simulation of thermally stratified atmospheric boundary-layer flow using a minimum dissipation model. *Boundary-Layer Meteorology*, *165*, 405–419. doi: 10.1007/s10546-017-0288-4

Angevine, W. M., Jiang, H., & Mauritsen, T. (2010). Performance of an eddy diffusivity–mass flux scheme for shallow cumulus boundary layers. *Monthly Weather Review*, *138*, 2895–2912.

Arakawa, A. (2004). The cumulus parameterization problem: past, present, and future. *Journal of Climate*, *17*, 2493–2525. doi: 10.1175/1520-0442(2004)017⟨2493:RATCPP⟩2.0.CO;2

Augier, P., Chomaz, J.-M., & Billant, P. (2012). Spectral analysis of the transition to turbulence from a dipole in stratified fluid. *Journal of Fluid Mechanics*, *713*, 86–108. doi: 10.1017/jfm.2012.437

Beare, R. J., Macvean, M. K., Holtslag, A. A. M., Cuxart, J., Esau, I., Golaz, J.-C., ... Sullivan, P. (2006). An intercomparison of large-eddy simulations of the stable boundary layer. *Boundary-Layer Meteorology*, *118*, 247–272. doi: 10.1007/s10546-004-2820-6

Beljaars, A. C. M. (1995). The parametrization of surface fluxes in large-scale models under free convection. *Quarterly Journal of the Royal Meteorological Society*, *121*, 255–270. doi: 10.1002/qj.49712152203

Billant, P., & Chomaz, J.-M. (2001). Self-similarity of strongly stratified inviscid flows. *Physics of Fluids*, *13*, 1645-1651. doi: 10.1063/1.1369125

Bjerknes, J. (1938). Saturated-adiabatic ascent of air through dry-adiabatically descending environment. *Quarterly Journal of the Royal Meteorological Society*, *64*, 325–330.

Blackadar, A. K. (1962). The vertical distribution of wind and turbulent exchange in a neutral atmosphere. *Journal of Geophysical Research*, *67*, 3095–3102. doi: 10.1029/JZ067i008p03095

Bougeault, P. (1981). Modeling the trade-wind cumulus boundary layer. Part I: Testing the ensemble cloud relations against numerical data. *Journal of the Atmospheric Sciences*, *38*, 2414–2428. doi: 10.1175/1520-0469(1981)038⟨2414:MTTWCB⟩2.0.CO;2

Bryan, G. H., & Fritsch, J. M. (2002). A benchmark simulation for moist nonhydrostatic numerical models. *Monthly Weather Review*, *130*, 2917–2928. doi: 10.1175/1520-0493(2002)130⟨2917:ABSFMN⟩2.0.CO;2

Businger, J. A., Wyngaard, J. C., Izumi, Y., & Bradley, E. F. (1971). Flux-profile relationships in the atmospheric surface layer. *Journal of the Atmospheric Sciences*, *28*, 181–189. doi: 10.1175/1520-0469(1971)028⟨0181:FPRITA⟩2.0.CO;2

Byun, D. W. (1990). On the analytical solutions of flux-profile relationships for the atmospheric surface layer. *Journal of Applied Meteorology*, *29*, 652–657. doi: 10.1175/1520-0450(1990)029⟨0652:OTASOF⟩2.0.CO;2

Cohen, Y., Lopez-Gomez, I., Jaruga, A., He, J., Kaul, C., & Schneider, T. (2020). Unified entrainment and detrainment closures for extended eddy-diffusivity mass-flux schemes. *Preprint on https://essoar.org*. doi: 10.1002/essoar.10502905.1.

Collins, W. D., Rasch, P. J., Boville, B. A., Hack, J. J., McCaa, J. R., Williamson, D. L., ... others (2004). Description of the NCAR community atmosphere model (CAM 3.0). *NCAR Technical Note NCAR/TN-464+ STR*, *226*.

Curry, J. A., Pinto, J. O., Benner, T., & Tschudi, M. (1997). Evolution of the cloudy boundary layer during the autumnal freezing of the Beaufort Sea. *Journal of Geophysical Research: Atmospheres*, *102*, 13851-13860. doi: 10.1029/96JD03089

Davini, P., D'Andrea, F., Park, S.-B., & Gentine, P. (2017). Coherent structures in large-eddy simulations of a nonprecipitating stratocumulus-topped boundary layer. *Journal of the Atmospheric Sciences*, *74*, 4117–4137. doi: 10.1175/JAS-D-17-0050.1

Grachev, A. A., Andreas, E. L., Fairall, C. W., Guest, P. S., & Persson, P. O. G. (2013). The critical Richardson number and limits of applicability of local similarity theory in the stable boundary layer. *Boundary-Layer Meteorology*, *147*, 51–82. doi: 10.1007/s10546-012-9771-0

Gregory, D. (2001). Estimation of entrainment rate in simple models of convective clouds. *Quarterly Journal of the Royal Meteorological Society*, *127*, 53-72.

Grisogono, B. (2010). Generalizing 'z-less' mixing length for stable boundary layers. *Quarterly Journal of the Royal Meteorological Society*, *136*, 213-221. doi: 10.1002/qj.529

Han, J., & Bretherton, C. S. (2019). TKE-based moist eddy-diffusivity mass-Flux (EDMF) parameterization for vertical turbulent mixing. *Weather and Forecasting*. doi: 10.1175/WAF-D-18-0146.1

He, Y., McFarlane, N. A., & Monahan, A. H. (2019). A new TKE-based parameterization of atmospheric turbulence in the Canadian global and regional climate models. *Journal of Advances in Modeling Earth Systems*, *11*.

Kajikawa, Y., Miyamoto, Y., Yoshida, R., Yamaura, T., Yashiro, H., & Tomita, H. (2016). Resolution dependence of deep convections in a global simulation from over 10-kilometer to sub-kilometer grid spacing. *Progress in Earth and Planetary Science*, *3*, 16. doi: 10.1186/s40645-016-0094-5

Katul, G. G., Li, D., Chamecki, M., & Bou-Zeid, E. (2013). Mean scalar concentration profile in a sheared and thermally stratified atmospheric surface layer. *Physical Review E*, *87*, 023004. doi: 10.1103/PhysRevE.87.023004

Lappen, C.-L., & Randall, D. A. (2001). Toward a unified parameterization of the boundary layer and moist convection. part I: A new type of mass-flux model. *Journal of the Atmospheric Sciences*, *58*, 2021-2036. doi: 10.1175/1520-0469(2001)058⟨2021:TAUPOT⟩2.0.CO;2

Li, D. (2019). Turbulent Prandtl number in the atmospheric boundary layer - where are we now? *Atmospheric Research*, *216*, 86–105. doi: https://doi.org/10.1016/j.atmosres.2018.09.015

Li, D., Salesky, S. T., & Banerjee, T. (2016). Connections between the Ozmidov scale and mean velocity profile in stably stratified atmospheric surface layers. *Journal of Fluid Mechanics*, *797*, R3. doi: 10.1017/jfm.2016.311

Lilly, D. K. (1968). Models of cloud-topped mixed layers under a strong inversion. *Quarterly Journal of the Royal Meteorological Society*, *94*, 292–309. doi: 10.1002/qj.49709440106

Mellor, G. L. (1977). The Gaussian cloud model relations. *Journal of the Atmospheric Sciences*, *34*, 356–358. doi: 10.1175/1520-0469(1977)034⟨0356:TGCMR⟩2.0.CO;2

Mellor, G. L., & Yamada, T. (1982). Development of a turbulence closure model for geophysical fluid problems. *Reviews of Geophysics*, *20*, 851–875. doi: 10.1029/RG020i004p00851

Monin, A., & Obukhov, A. (1954). Basic laws of turbulent mixing in the surface layer of the atmosphere. *Trudy Akademii Nauk SSSR Geofizicheskii Institut*, *24*, 163–187.

Nakanishi, M. (2001). Improvement of the Mellor-Yamada turbulence closure model based on large-eddy simulation data. *Boundary-Layer Meteorology*, *99*, 349–378. doi: 10.1023/A:1018915827400

Nieuwstadt, F. T. M., Mason, P. J., Moeng, C.-H., & Schumann, U. (1993). Large-eddy simulation of the convective boundary layer: A comparison of four computer codes. In F. Durst, R. Friedrich, B. E. Launder, F. W. Schmidt, U. Schumann, & J. H. Whitelaw (Eds.), (pp. 343–367). Berlin, Heidelberg: Springer Berlin Heidelberg.

O'Gorman, P. A. (2010). The effective static stability experienced by eddies in a moist atmosphere. *Journal of the Atmospheric Sciences*, *68*, 75–90. doi: 10.1175/2010JAS3537.1

Optis, M., Monahan, A., & Bosveld, F. C. (2016). Limitations and breakdown of Monin–Obukhov similarity theory for wind profile extrapolation under stable stratification. *Wind Energy*, *19*, 1053–1072. doi: 10.1002/we.1883

Park, S. (2014). A unified convection scheme (UNICON). Part I: Formulation. *Journal of the Atmospheric Sciences*, *71*, 3902-3930. doi: 10.1175/JAS-D-13-0233.1

Pressel, K. G., Kaul, C. M., Schneider, T., Tan, Z., & Mishra, S. (2015). Large-eddy simulation in an anelastic framework with closed water and entropy balances. *Journal of Advances in Modeling Earth Systems*, *7*, 1425–1456. doi: 10.1002/2015MS000496

Pressel, K. G., Mishra, S., Schneider, T., Kaul, C. M., & Tan, Z. (2017). Numerics and subgrid-scale modeling in large eddy simulations of stratocumulus

clouds. *Journal of Advances in Modeling Earth Systems*, *9*, 1342–1365. doi: 10.1002/2016MS000778

Randall, D. A. (2013). Beyond deadlock. *Geophysical Research Letters*, *40*, 5970–5976. doi: 10.1002/2013GL057998

Romps, D. M., & Charn, A. B. (2015). Sticky thermals: Evidence for a dominant balance between buoyancy and drag in cloud updrafts. *Journal of the Atmospheric Sciences*, *72*(8), 2890–2901. Retrieved from `https://doi.org/10.1175/JAS-D-15-0042.1` doi: 10.1175/JAS-D-15-0042.1

Schneider, T., Teixeira, J., Bretherton, C. S., Brient, F., Pressel, K. G., Schär, C., & Siebesma, A. P. (2017). Climate goals and computing the future of clouds. *Nature Climate Change*, *7*.

Schubert, W. H. (1976). Experiments with Lilly's cloud-topped mixed layer model. *Journal of the Atmospheric Sciences*, *33*, 436–446. doi: 10.1175/1520-0469(1976)033⟨0436:EWLCTM⟩2.0.CO;2

Schumann, U., & Moeng, C.-H. (1991). Plume budgets in clear and cloudy convective boundary layers. *Journal of the Atmospheric Sciences*, *48*, 1758–1770. doi: 10.1175/1520-0469(1991)048⟨1758:PBICAC⟩2.0.CO;2

Siebesma, A. P., Soares, P. M. M., & Teixeira, J. (2007). A combined eddy-diffusivity mass-flux approach for the convective boundary layer. *Journal of the Atmospheric Sciences*, *64*, 1230–1248. doi: 10.1175/JAS3888.1

Siebesma, A. P., & Teixeira, J. (2000). An advection-diffusion scheme for the convective boundary layer: description and 1d-results. *Proceedings of the 14th AMS Symposium on Boundary Layers and Turbulence*, 133-136.

Soares, P. M. M., Miranda, P. M. A., Siebesma, A. P., & Teixeira, J. (2004). An eddy-diffusivity/mass-flux parametrization for dry and shallow cumulus convection. *Quarterly Journal of the Royal Meteorological Society*, *130*, 3365-3383. doi: 10.1256/qj.03.223

Sommeria, G., & Deardorff, J. W. (1977). Subgrid-scale condensation in models of nonprecipitating clouds. *Journal of the Atmospheric Sciences*, *34*, 344-355. doi: 10.1175/1520-0469(1977)034⟨0344:SSCIMO⟩2.0.CO;2

Sorbjan, Z., & Grachev, A. A. (2010). An evaluation of the flux–gradient relationship in the stable boundary layer. *Boundary-Layer Meteorology*, *135*(3), 385–405. doi: 10.1007/s10546-010-9482-3

Spalart, P. R. (1988). Direct simulation of a turbulent boundary layer up to Rθ = 1410. *Journal of Fluid Mechanics*, *187*, 61–98. doi: 10.1017/S0022112088000345

Stevens, B., Lenschow, D. H., Vali, G., Gerber, H., Bandy, A., Blomquist, B., ... van Zanten, M. C. (2003). Dynamics and chemistry of marine stratocumulus - DYCOMS-II. *Bulletin of the American Meteorological Society*, *84*, 579–594. doi: 10.1175/BAMS-84-5-579

Stevens, B., Moeng, C.-H., Ackerman, A. S., Bretherton, C. S., Chlond, A., de Roode, S., ... Zhu, P. (2005). Evaluation of large-eddy simulations via observations of nocturnal marine stratocumulus. *Monthly Weather Review*, *133*, 1443-1462. doi: 10.1175/MWR2930.1

Suselj, K., Teixeira, J., & Chung, D. (2013). A unified model for moist convective boundary layers based on a stochastic eddy-diffusivity/mass-flux parameterization. *Journal of the Atmospheric Sciences*, *70*, 1929-1953. doi: 10.1175/JAS-D-12-0106.1

Tan, Z., Kaul, C. M., Pressel, K. G., Cohen, Y., Schneider, T., & Teixeira, J. (2018). An extended eddy-diffusivity mass-flux scheme for unified representation of subgrid-scale turbulence and convection. *Journal of Advances in Modeling Earth Systems*, *10*, 770-800. doi: 10.1002/2017MS001162

Thuburn, J., Weller, H., Vallis, G. K., Beare, R. J., & Whitall, M. (2018). A framework for convection and boundary layer parameterization derived from conditional filtering. *Journal of the Atmospheric Sciences*, *75*, 965–981. doi:

10.1175/JAS-D-17-0130.1

Titsias, M. K. (2016). One-vs-each approximation to softmax for scalable estimation of probabilities. In *Proceedings of the 30th international conference on neural information processing systems* (pp. 4168–4176). USA: Curran Associates Inc.

Umlauf, L., & Burchard, H. (2003). A generic length-scale equation for geophysical turbulence models. *Journal of Marine Research*, *61*, 235-265. doi: 10.1357/002224003322005087

Vassilicos, J. C. (2015). Dissipation in turbulent flows. *Annual Review of Fluid Mechanics*, *47*, 95–114. doi: 10.1146/annurev-fluid-010814-014637

Verstappen, R. (2011). When does eddy viscosity damp subfilter scales sufficiently? *Journal of Scientific Computing*, *49*, 94. doi: 10.1007/s10915-011-9504-4

Waite, M. L. (2011). Stratified turbulence at the buoyancy scale. *Physics of Fluids*, *23*(6), 66602. doi: 10.1063/1.3599699

Witek, M. L., Teixeira, J., & Matheou, G. (2011). An integrated TKE-based eddy diffusivity/mass flux boundary layer closure for the dry convective boundary layer. *Journal of the Atmospheric Sciences*, *68*, 1526-1540. doi: 10.1175/2011JAS3548.1

Wu, E., Yang, H., Kleissl, J., Suselj, K., Kurowski, M. J., & Teixeira, J. (2020). On the parameterization of convective downdrafts for marine stratocumulus clouds. *Monthly Weather Review*, *148*, 1931-1950. doi: 10.1175/MWR-D-19-0292.1